Time-resolved cryo-EM visualizes ribosomal translocation with EF-G and GTP

Christine E. Carbone[1], Anna B. Loveland[1], Howard Gamper Jr.[2], Ya-Ming Hou[2], Gabriel Demo[1,3,#], Andrei A. Korostelev[1,#]

[1]RNA Therapeutics Institute, Department of Biochemistry and Molecular Pharmacology, UMass Medical School, Worcester, MA, USA

[2]Department of Biochemistry and Molecular Biology, Thomas Jefferson University, Philadelphia, PA, USA

[3]Central European Institute of Technology, Masaryk University, Kamenice 5, Brno, 625 00, Czech Republic

[#]Correspondence: gabriel.demo@ceitec.muni.cz and Andrei.Korostelev@umassmed.edu

Abstract

During translation, a conserved GTPase elongation factor—EF-G in bacteria or eEF2 in eukaryotes—translocates tRNA and mRNA through the ribosome. EF-G has been proposed to act as a flexible motor that propels tRNA and mRNA movement, as a rigid pawl that biases unidirectional translocation resulting from ribosome rearrangements, or by various combinations of motor- and pawl-like mechanisms. Using time-resolved cryo-EM, we visualized GTP-catalyzed translocation without inhibitors, capturing elusive structures of ribosome•EF-G intermediates at near-atomic resolution. Prior to translocation, EF-G binds near peptidyl-tRNA, while the rotated 30S subunit stabilizes the EF-G GTPase center. Reverse 30S rotation releases Pi and translocates peptidyl-tRNA and EF-G by ~20 Å. An additional 4-Å translocation initiates EF-G dissociation from a transient ribosome state with highly swiveled 30S head. The structures visualize how nearly rigid EF-G rectifies inherent and spontaneous ribosomal dynamics into tRNA-mRNA translocation, whereas GTP hydrolysis and Pi release drive EF-G dissociation.

Introduction

Continuous protein synthesis depends on synchronous translocation of mRNA and tRNAs through the ribosome (reviewed in refs [1-6]). After peptide bond formation, the pre-translocation ribosome contains peptidyl-tRNA in the A (aminoacyl-tRNA) site and deacyl-tRNA in the P (peptidyl-tRNA) site, which must be translocated with their mRNA codons to the P and E (exit) sites, respectively (Fig. 1a). The pre-translocation ribosome samples two globally different conformations, which interconvert spontaneously. These are the non-rotated and rotated conformation [7-10], in which the small subunit is rotated by up to 10° [11,12]. In the rotated ribosome, the tRNA anticodon stem loops (ASLs) remain bound to the mRNA codons in the A and P sites on the small subunit, while the acceptor arms of tRNAs are shifted into the P and E sites of the large subunit [7-9,13-16], thus adopting hybrid states denoted as A/P peptidyl-tRNA and P/E deacyl-tRNA [17,18]. In the next translocation step, the ASLs and mRNA shift along the 30S subunit, forming a post-translocation ribosome—with P-site peptidyl-tRNA and E-site deacyl-tRNA—prepared to accept the next aminoacyl-tRNA and continue the elongation cycle [19].

Translocation of the ASLs and mRNA along the 30S subunit is catalyzed by a conserved GTPase, elongation factor G (EF-G) in bacteria or EF-2 in archaea and eukaryotes (Fig. 1a). The structural mechanism of translocation has not been visualized because the rapid GTP hydrolysis step has prevented the capture of authentic EF-G-bound structural intermediates. Prior studies relied on stalling EF-G on the ribosome by antibiotics [20-24], EF-G mutations [25,26] or non-hydrolyzable GTP analogs [27-29], which might capture off-pathway states [30]. Structural studies captured ribosome•EF-G conformations ranging from rotated pre-translocation-like [20] through mid-rotated [21-23] to non-rotated post-translocation-like [24] or non-rotated pre-translocation-like states [26]. The structural relationship between GTP hydrolysis, EF-G rearrangements and translocation, however, remains uncharacterized, as some stalled structures may be inconsistent with the biochemical progression of translocation. For example, a crystallographic pre-translocation-like ribosome structure captured mutant EF-G with GDP [26], whereas in solution, pre-translocation ribosomes bind EF-G•GTP [31,32]. Furthermore, post-translocation ribosomes were reported with GTP-bound-like conformations of mutant EF-G or of EF-G with GTP analogs [25,28], whereas authentic post-translocation states must feature post-GTP-hydrolysis states of EF-G.

Two groups of mechanistic models, as well as their combinations, have been suggested to explain EF-G•GTP-catalyzed translocation. In the first group of mechanisms, the energy of GTP hydrolysis is proposed to directly contribute to translocation [33,34] by causing a large-scale conformational change of EF-G [26,35] to exert force [36-38] and/or by inducing ribosome rearrangements that propel tRNA movement [10,30,39]. A ribosome crystal structure with a compact EF-G mutant fused with L9 suggested a nearly 100-Å inter-domain movement [26] toward an extended EF-G conformation captured in most structural studies, in keeping with EF-G acting as a flexible motor. The second group of mechanistic models argues that EF-G acts as a steric hindrance, or pawl, that rectifies the inherent thermal motions of the ribosome, including

spontaneous interconversion between non-rotated and rotated conformations, into tRNA translocation [40,41]. These models are consistent with the ribosome's ability to slowly translocate tRNA in the absence of EF-G [42-45], indicating that translocation is an inherent property of the ribosome. Because non-hydrolyzable GTP analogs efficiently catalyze translocation, accelerating it by more than 10^3-fold [19,33,39,46], the translocation stage was proposed to be independent of GTP hydrolysis and large-scale interdomain rearrangements of EF-G [20]. Nevertheless, the rate of translocation in the presence of EF-G and GTP is up to 50-fold higher than with GTP analogs or catalytically inactive EF-G [19,25,33,39,47]. Thus, neither group of models fully explains the structural roles of EF-G and GTP hydrolysis [1,34].

To understand how EF-G and GTP catalyze translocation, we performed time-resolved cryogenic electron microscopy to visualize authentic translocation intermediates without inhibitors (Fig. 1 and Figs. S1-2). We report three ribosome intermediates with EF-G (Fig. 1A-B), resolving the EF-G's GTPase center at ~3 Å local resolution (Fig. 1H and Fig. S3). Together with the pre-translocation and post-translocation states observed without EF-G, our data allow reconstruction of the structural pathway of translocation, elucidating the structural roles of EF-G (Figs. 2 and 3) and GTP hydrolysis (Fig. 4). In addition to inhibitor-free complexes, we report a 3.2-Å structure of a pre-translocation complex formed with EF-G•GTP and stalled with viomycin, which supports our findings (Figs. S2 and S3). Comparison with previous structural studies suggests that some conformations of EF-G or ribosomes stalled by GTP analogs, antibiotics and mutations, may represent the states that are lowly-populated or not populated during GTP-catalyzed translocation.

Results and Discussion

Cryo-EM captures EF-G•GTP translocation intermediates

To visualize EF-G-catalyzed translocation using time-resolved cryo-EM, we added *E. coli* EF-G•GTP to pre-translocation 70S ribosomes with $tRNA^{fMet}$ in the P site and with dipeptidyl-$tRNA^{Pro}$ in the A site programmed with the cognate CCA codon (Fig. 1a; Methods). The reaction was performed on ice to slow translocation [44] and enable capturing translocation intermediates. We plunged EM grids into a cryogen to stop the reaction at 0 (prior to adding EF-G•GTP), 25, and 3600 seconds, and collected cryo-EM data for each time point. Maximum-likelihood classification of ribosome particles in these datasets identified nine structures, comprising three major functional states of the ribosome: pre-translocation substrates, EF-G-bound intermediates, and post-translocation products (Figs. 1b and S1). As the population of pre-translocation ribosomes decreases over time, the population of post-translocation ribosomes increases, as expected. EF-G-bound intermediates were only observed in data from the intermediate time point (Fig. 1c).

The pre-translocation substrates, obtained without EF-G, feature four conformations of the ribosome and tRNAs: non-rotated Structure I and rotated Structures II-A through II-C (Figs. 1b and S4). Structure I contains tRNAs in the classical A (A/A) and P (P/P) states, and a low-occupancy E-site (Fig. S4a), similar to those in previous studies of elongation [48] (e.g. Structure V-B in ref 53). Structure II-A features a rotated ribosome with an A/A-like $tRNA^{Pro}$ and P/E $tRNA^{fMet}$ (Figs. S4b and S5a-b). This state reveals that upon intersubunit rotation, dipeptidyl-tRNA can remain in the 50S A site while the acceptor arm of the deacyl-tRNA shifts to the E site, as suggested by studies using Fluorescence/Förster Resonance Energy Transfer (FRET) [15], mutant bacterial ribosomes [49], mitochondrial ribosomes [50], and ribosomes with fungi-specific eEF3 [51]. Structure II-B features a rotated ribosome with canonical A/P and P/E hybrid-state tRNAs, whose acceptor arms are shifted to the P and E sites on the large subunit (Figs. S4c and S5), resembling Structure VI-A in ref 53 and hybrid-state tRNAs in most other studies [14,52]. In Structure II-C (similar to VI-B in ref 53), the elbow of A/P* tRNA is shifted by ~25 Å toward the P site (Figs. S4d and S5). Similar tRNA conformations, including the A/P and A/P* tRNA, are sampled by other tRNA species (e.g. $tRNA^{Phe}$) on pre-translocation ribosomes from bacteria [53] and eukaryotes [54,55], in keeping with the conservation of ribosomal and tRNA rearrangements during the elongation cycle. Our structures I through II-C confirm that prior to translocation, the ASL of peptidyl-tRNA remains in the 30S A site, whereas the acceptor arm and elbow spontaneously sample different conformations, including the A/P* state, which is most advanced toward the P site.

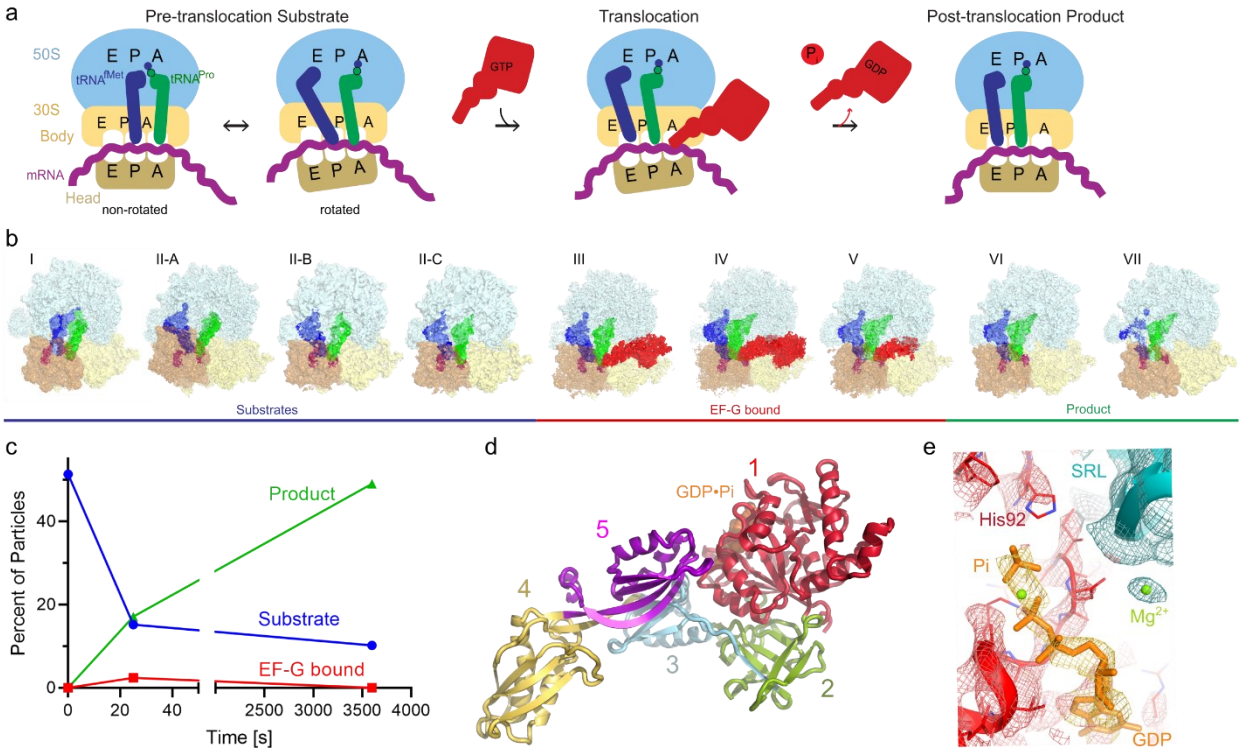

Figure 1. Time-resolved cryo-EM of translocation with EF-G and GTP. a, Scheme of the translocation reaction of the 70S•mRNA•fMet-tRNA^{fMet}•Pro-tRNA^{Pro} complex with EF-G•GTP. **b**, Segmented cryo-EM maps of 9 states of the translocation reaction, and their assignment as substrates, EF-G-bound intermediates, or products of the reaction. The maps are colored to show the 50S ribosomal subunit (light blue), 30S ribosomal subunit (yellow), tRNA^{fMet} (dark blue), tRNA^{Pro} (green), mRNA (magenta) and EF-G (red). **c**, Relative abundance of substrates, EF-G intermediates and translocation products over time, obtained from particle distributions in cryo-EM datasets. **d**, Domain organization of EF-G; Arabic numerals denote the five conserved domains of the elongation factor. **e**, Cryo-EM density of the EF-G GTPase center in the transient pre-translocation and pre-Pi-release state (III). For additional density views, see Figs. 4, S3, S4 and S5.

Three structures of transient translocation intermediates (III, IV and V) include long-sought EF-G-bound states resolved at ~3.5 Å average resolution. These structures represent distinct stages of tRNA advancement along the translocation trajectory (Fig. 2). Structure III features a pre-translocation 70S•EF-G complex with A/P* and P/E tRNAs (Fig. 2a). In Structure IV, EF-G is shifted ~20 Å along the 30S subunit, with partially translocated “chimeric” ap/P and pe/E tRNAs (Fig. 2b; tRNA nomenclature as in [23]). In Structure V, tRNA ASLs are further along the translocation pathway, reaching the P and E sites of the 30S body domain (we term the tRNAs ap*/P and pe*/E; Fig. 2c). EF-G translocase domain shifts with the tRNAs by another 4 Å, but the N-terminal domains 1 and 2 are unresolved (Fig. 2c) indicating that they have dissociated from the ribosome and are dynamic in the intersubunit space.

Two post-translocation products (VI and VII) lack EF-G. The ribosome with a highly swiveled 30S head and ap*/P and pe*/E tRNAs in Structure VI is nearly identical to the EF-G-bound Structure V. Structure VI is found exclusively in the 25-second data set, indicating that it is

a transient state formed after EF-G dissociation. By contrast, the terminal post-translocation Structure VII with fully translocated dipeptidyl-tRNA^{Pro} in the P site is present in both the 25- and 3600-second data sets. Here, the non-rotated ribosome with a non-swiveled head is nearly identical to Structure I (Fig. 2h) and previous structures of post-translocation complexes [48,56], and the ribosome is ready for the next round of elongation.

Extended EF-G binds rotated pre-translocation ribosomes with A/P* tRNA

During translocation, the ASL of peptidyl-tRNA with its mRNA codon must traverse a ~25 Å distance from the A to P site (measured between codon nucleotide-34 phosphates of A- and P-site tRNAs). This movement is accompanied by the reverse ~10° rotation of the 30S subunit body [19]. Moreover, ribosome structures with inhibitors [23,57-60], and solution FRET studies [7,61], reported that EF-G or eEF-2 binding is associated with a large, up to ~20°, rotation ("swivel") of the head domain of the small subunit. However, authentic EF-G-bound translocation intermediates with rotated body or swiveled head have eluded structural characterization.

Structure III (Fig. 2a) reveals EF-G bound to a fully rotated ribosome with A/P* tRNA, similar to pre-translocation Structure II-C captured prior to EF-G binding (Fig. 2h and Table S2). Superposition with other rotated pre-translocation states reveals that EF-G is incompatible with Structures II-A and II-B (Fig. S5e-f), because tRNAs in the A/A and A/P conformations would clash with the EF-G translocase domain 4 (aa 490-610; *E.coli* numbering; Arabic numerals are used for EF-G domain designation as in ref [62]). These observations indicate that the spontaneously sampled ribosome with A/P* tRNA is the substrate for EF-G binding.

In Structure III, EF-G adopts an extended conformation in the intersubunit space, spanning 100 Å from the GTPase domain to the tip of domain 4 (Figs. 1d, 2a). The GTPase domain (domain 1, also termed the G-domain; aa 1-290; Fig. 1d) binds at the universally conserved sarcin-ricin loop of the large subunit (SRL; nucleotides 2653–2667 of 23S rRNA). In its vicinity, EF-G domain 5, which forms the translocase superdomain with domain 4, binds to the L11 stalk (23S residues 1050-1105 and protein L11; Figs. 2a and S6a). Domains 2 and 3 (part of the GTPase superdomain) bind at a peripheral region of the 30S shoulder and body domains (Fig. 2a).

EF-G domain 4 is inserted between dipeptidyl-tRNA^{Pro}, the 30S shoulder and the 30S head domains (Fig. 2a). Loop 1 at the tip of domain 4 (aa 507-514) is wedged between the tRNA and decoding center, where it reaches toward the 16S nucleotide G530 on the 30S shoulder (Figs. 3a and S6b-c), one of the three universally conserved nucleotides critical for mRNA decoding and A-site-tRNA stabilization or "locking" [53,63-66]. The neighboring loop 2 (aa 582-588) fits into a minor groove of helix 34 of 16S rRNA (at C1209), binding the 30S head in a pre-swiveled conformation. Thus, domain 4 is positioned to separate, or "unlock", the codon-anticodon helix from the decoding center and follow the head during translocation.

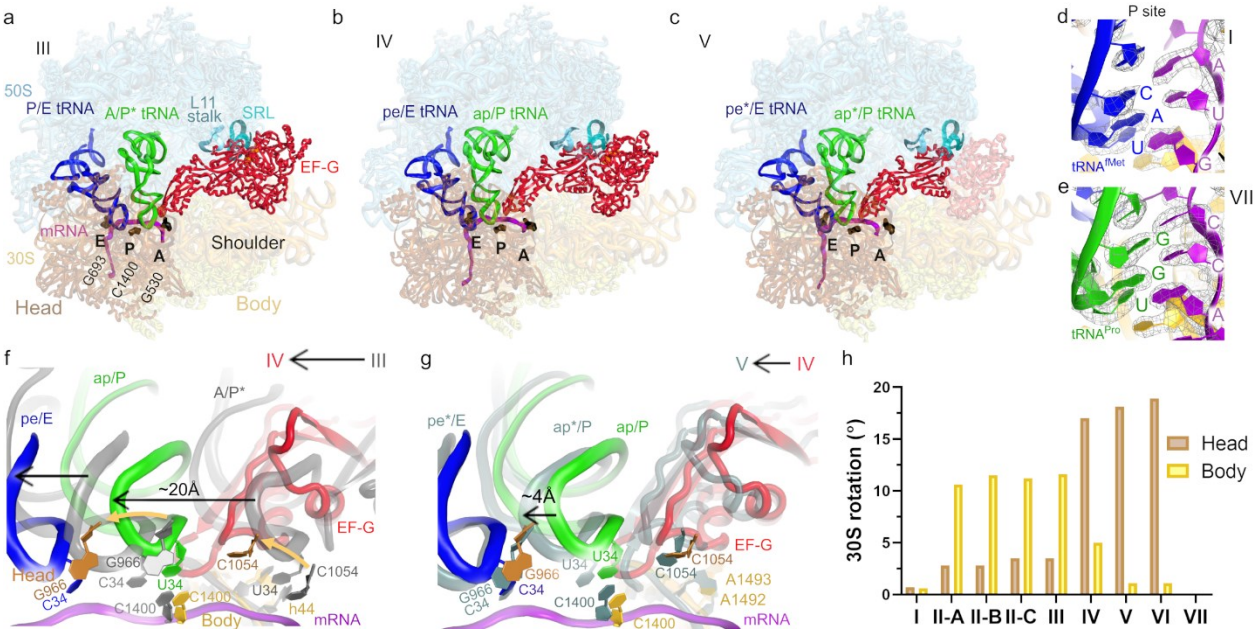

Figure 2. Structures of translocation intermediates with EF-G. a-c, Structures III, IV and V with EF-G. 16S nucleotides at the A, P and E sites (G530, C1400 and G693, respectively) are shown as black surfaces for reference. Unresolved part of EF-G in Structure V is shown in transparent red in panel c. **d-e,** high-resolution density showing pre-translocation (**d**) and post-translocation (**e**) positions of tRNA and mRNA codon in the P sites of Structures I and VII. **f-g,** Transitions of tRNA and EF-G between Structures III and IV (**f**) and Structures IV and V (**g**). **h,** Degrees of 30S head swivel and body rotation in Structures I through VII.

Nearly rigid EF-G enters the A site during reverse 30S body rotation

In the mid-translocation Structure IV, EF-G retains an extended conformation, similar to that in Structure III, with EF-G domain 5 anchored to the L11 stalk of the 50S subunit (Fig. 2b). Because the 30S body has reversed its rotation to 5.0° (from 11.6° in Structure III, Table S2), EF-G domains 2 to 4 have moved along the 30S subunit (Fig. S6d-e). Domain 4 is shifted 20-Å (measured at Tyr 515 near loop 1) from its position in Structure III, inserting into the A site (Fig. 2f and 3b). Loop 1 has moved to contact nucleotides of both the CCA codon and the dipeptidyl-tRNA^{Pro} anticodon (Fig. S6f-g). In this position, domain 4 separates the tRNA from the decoding-center nucleotides (Fig. 3b). The ASL of dipeptidyl-tRNA^{Pro} is translocated 18-Å relative to the 30S body, so that the anticodon nucleotide U34 stacks on the 30S P-site residue C1400 of 16S rRNA (Fig. 2f). However, due to a 17° swivel of the 30S head toward the large subunit (i.e., in the direction of translocation), dipeptidyl-tRNA remains near the A site of the 30S head, and deacyl-tRNA^{fMet} remains near the P-site of the 30S head, where C34 stacks on G966 of 16S rRNA (Figs. 2f and S6e). These tRNA conformations closely resemble chimeric ap/P and pe/E tRNAs captured in the presence of fusidic acid or neomycin [21,23]. Unlike in the neomycin-bound high-resolution structure, in which the tRNA acceptor arm is between the 50S A and P sites [21], Structure IV features the acceptor arm of the

ap/P tRNA bound to the P loop of the 50S P site, similar to those of the hybrid-state P/E and translocated P-site tRNAs (Fig. S5c-d).

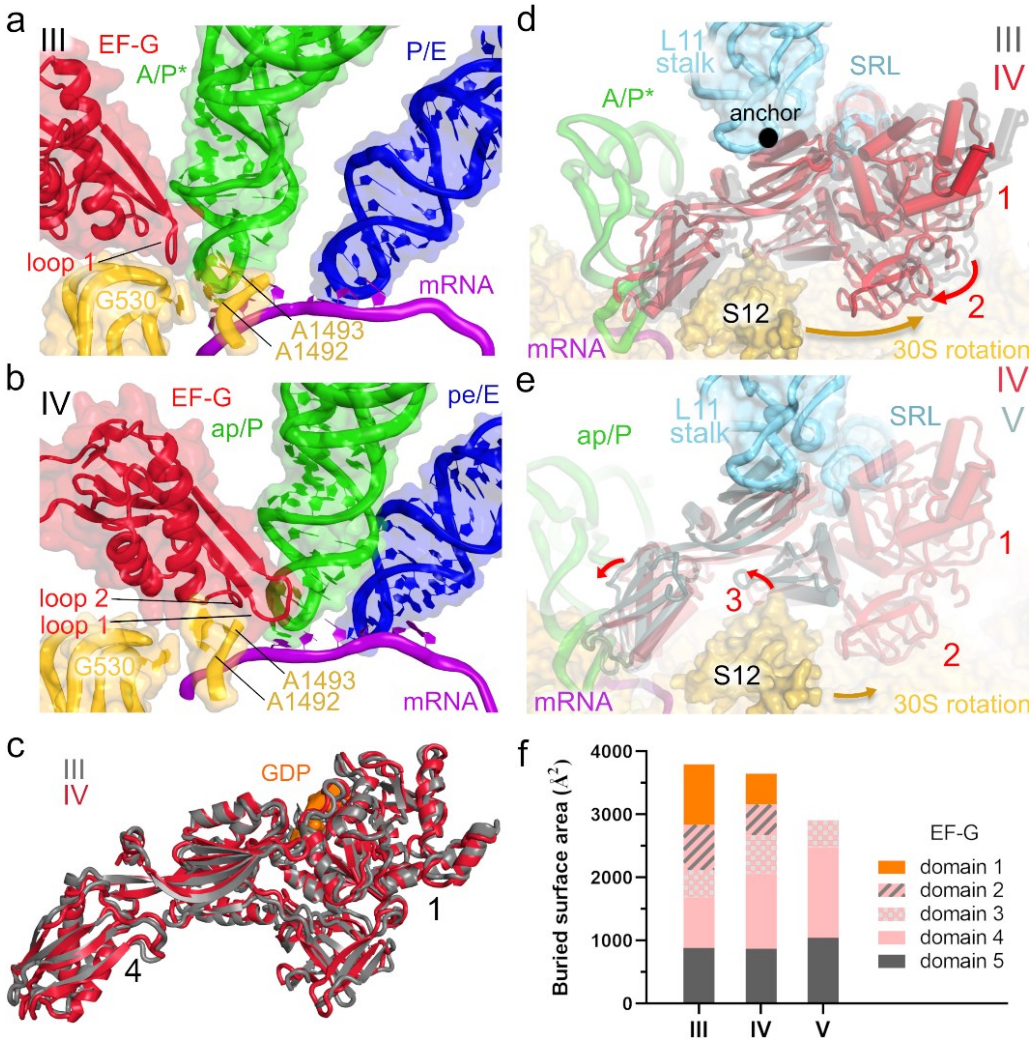

Figure 3. Positions and interactions of EF-G in translocation intermediates. a-b, positions of EF-G and tRNAs relative to the decoding center (yellow) in Structures III and IV. **c,** superposition of EF-G in Structures III and IV demonstrates an overall similar extended conformation. **d,** rearrangement of EF-G relative to the 30S subunit from Structure III (gray) to IV (colored). **e,** rearrangement of EF-G relative to the 30S subunit from Structure IV (colored) to V (blue-gray). **f,** Buried surface area (contact area) showing the extent of interactions of EF-G domains with the ribosome, mRNA, and/or tRNA in Structures III to V.

To accommodate into the A site, EF-G undergoes small-scale rearrangements (Fig. 3c), as domain 4 shifts relative to the GTPase domain by ~7 Å (RMSD, root-mean-square distance between superimposed EF-G from Structures III and IV). The range of interdomain rearrangements is similar to or less than interdomain fluctuations of free EF-G in solution [67] and in crystal structures of free EF-G homologs [62,68,69] (up to ~20 Å; Fig. S7), suggesting that EF-G undergoes local stochastic rearrangements to accommodate in the A site during translocation.

Structure V represents a heretofore unseen EF-G-bound ribosome state with a highly swiveled head and further translocated tRNAs (Figs. 2c, 2g). 30S body is less rotated (1.1°) than than that in Structure IV, whereas head swivel (18.1°) is slightly increased (Fig. 2h). EF-G domain 4 and tRNAs have advanced 3-5 Å along the 30S subunit. The ASL of dipeptidyl-tRNA^{Pro} is placed deeper into the P site of the 30S body, forming a late translocation state ap*/P (Figs. 2g and S6h). Strong density shows EF-G domain 4 occupying the ribosomal A site and domain 5 attached to the L11 stalk. Density for domain 3 is weaker, and densities for domains 1 and 2 are absent (Figs. 3e, S3d,h and S4g). Thus, Structure V is consistent with a late translocation intermediate, in which EF-G releases its hold on the ribosome, as the GTPase domain leaves the SRL and domain 2 leaves the 30S subunit. Dissociation of EF-G domains 1 and 2 correlates with steric hindrance presented by ribosomal protein S12 (Fig. 3e) and loss of interactions between domain 1 and the back-rotating 30S subunit, as discussed below. Step-wise dissociation of EF-G resembles that of EF-Tu, whose GTPase domain is released from the ribosome before other domains during tRNA decoding [53].

Structural analyses of EF-G-bound intermediates highlight that progression from Structure III to V is correlated with a stepwise loss of EF-G contact with the ribosome (Fig. 3f). Extensive interactions of the GTPase with the SRL and the small subunit in Structure III (GTPase-domain buried surface area of ~960 Å^2) are halved in Structure IV (493 Å^2) on the path to dissociation of the GTPase domain in Structure V (~0 Å^2). By contrast, the translocase superdomain expands its interactions with the ribosome. The invariant interaction of EF-G domain 5 with the L11 stalk of the 50S subunit in all three structures (~900 Å^2) holds EF-G in place to allow the entry into the A site during reverse 30S rotation. Interactions of domain 4 with the 30S subunit gradually expand from 800 Å^2 in Structure III through 1190 Å^2 in Structure IV to 1440 Å^2 in Structure V (Fig. 3f). Nevertheless, the overall contact area of EF-G during translocation reduces from 3730 Å^2 (whole EF-G buried surface area in Structure III) to 3530 Å^2 (IV; 95% from that in Structure III) to 2902 Å^2 (V; 77% from that in Structure III). Because the buried surface area positively correlates with the binding affinity of macromolecules [70], these measurements suggest that gradual dissociation of EF-G is driven by different affinities of EF-G to the ribosome in different 30S rotation/swivel states.

Structure VI lacks EF-G, but the tRNA positions and 30S conformation only marginally differ from those in Structure V (Figs. 1b and S4h). With a slightly more swiveled head (18.9°), Structure VI represents a transient translocation intermediate following EF-G dissociation.

The completion of tRNA and mRNA translocation along the head requires an ~20° reversal of head swivel, as in the post-translocation state captured in Structure VII (Figs. 1b and S4i). The non-rotated/non-swiveled Structure VII features an empty A site and tRNA^{Pro} with the associated proline codon clearly resolved in the P site (Figs. 2d-e). Very low density suggests that the bulk of deacyl-tRNA^{fMet} has dissociated from the E site (Figs. 1b and S4i). Extensive classification of cryo-EM data did not detect EF-G in non-rotated ribosomes that would resemble EF-G-bound structures stalled by fusidic acid [24], GTPase-defective EF-G mutant [25] or non-hydrolyzable GTP

analog [28]. Our structures therefore suggest that in the absence of inhibitors, EF-G dissociates before or during reversal of head swivel.

Pi release during tRNA translocation

Structures III and IV reveal two functional EF-G GTPase states distinguished by differing interactions with the 30S subunit and the SRL, which is essential for the hydrolysis of GTP [24,71-74]. Structure III features an activated GTPase domain clamped between the 30S and 50S subunits. The EF-G GTPase center is resolved to a local resolution of ~3 Å, allowing detailed interpretation of its conformation (Figs. 1e, 4a and S3b,f,j). Two switch loops (sw-I and sw-II) outline the GTP-binding pocket (Figs. S3 and S6i; [62,75,76]). The longer sw-I (aa 35-65) bridges the SRL with the small subunit, as described below. His44 of sw-I docks at G2655 of the SRL and stabilizes the ribose of GDP (Fig. 4d). On the opposite wall of the GTP-binding pocket, catalytic His92 of sw-II (aa 80-95) docks near the SRL at the phosphate of A2662, with its side chain oriented toward the γ-phosphate (inorganic phosphate, Pi, Fig. 4e) and Ile61 of sw-I, consistent with a catalytically activated GTPase [77]. This conformation contrasts with pre-GTP-hydrolysis states of free EF-G homologs [69,78], wherein His92 points away from γ-phosphate (Fig. 4e). Nevertheless, the overall fold of the GTPase center is remarkably similar to those in unbound GTPases (Fig. S6i), indicating that ribosome binding induces only a local rearrangement of His92 to activate GTP hydrolysis. Strong density suggests that the γ-phosphate is separated from GDP (Fig. 4a) and stabilized by hydrogen-bonding donors and positively charged side chains of sw-I and sw-II (Fig. S6j). The relative positions of Pi and GDP are nearly identical to those in high-resolution crystal structures of Ras GTPase and aIF2 (Fig. S6i; [79]). Moreover, the density is less compatible with GTP, whose covalently bound γ-phosphate would be closer to its β-phosphate (Fig.4a [69]). Thus, consistent with the fast chemical reaction [44,80,81], Structure III represents predominantly a post-GTP-hydrolysis step with GDP and Pi stabilized by the ordered switch loops.

Sw-I is sandwiched between the SRL and the 30S subunit, where His38 of sw-I packs on the bulged A344 residue in helix 14 of 16S rRNA (Fig. 4d). Helix 14 is closer to the SRL in the rotated ribosome (28 Å between the phosphates of A344 and A2662) than in the non-rotated conformation (36 Å), indicating that the rotated 30S conformation helps stabilize the active conformation of the GTPase center, leading to GTP hydrolysis (Fig. 4d). Indeed, the rotated pre-translocation ribosome is the authentic substrate for EF-G•GTP binding and hydrolysis [32,82], whereas an isolated SRL RNA oligonucleotide does not activate GTP hydrolysis on EF-G [72]. Moreover, by stabilizing sw-I, the rotated 30S prevents the release of the Pi, ensuring that EF-G does not dissociate prior to translocation.

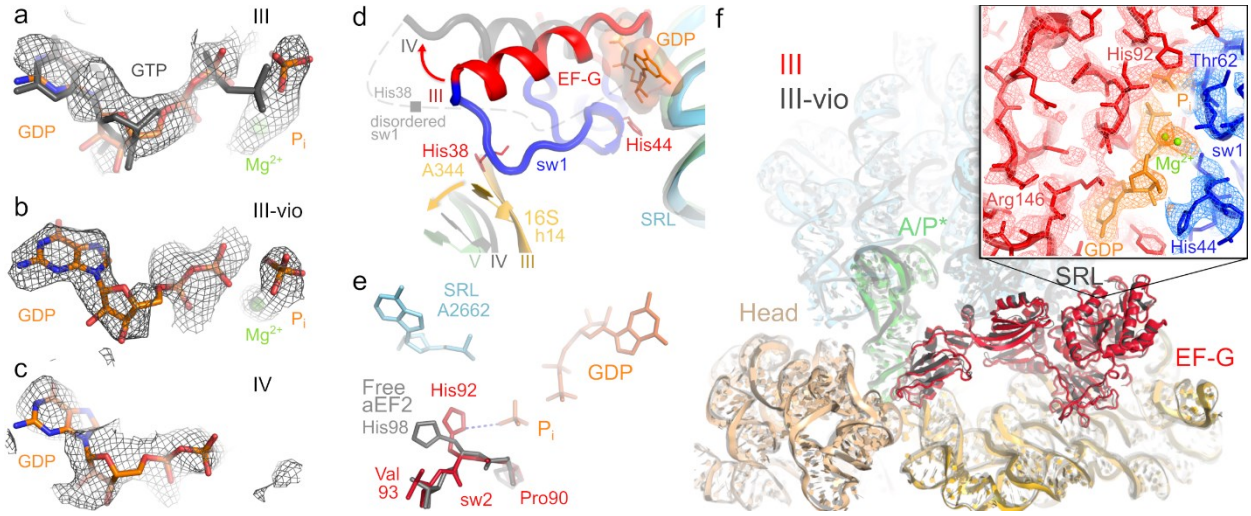

Figure 4. The GTPase center of EF-G in translocation Structures III, III-vio and IV. a-c, Cryo-EM densities are consistent with GDP•Pi in Structures III and III-vio, and with GDP in Structure IV. Grey model shows GTP for reference (1WDT). **d,** Positions of sw-I in Structure III (ordered) and IV (gray, disordered) between the SRL and h14 of the 30S subunit. **e,** The catalytic conformation of His92 in Structure III differs from position of this side chain in the off-ribosome EF-G homolog (archaeal EF-2) bound with GTP analog [78]. **f,** Pre-translocation 70S•EF-G•GDP•Pi structure captured with viomycin (III-vio; gray) is nearly identical to Structure III. Box shows density for EF-G GTPase center in Structure III-vio (His92 density is shown in Fig. S2c).

Overall, Structure III resembles a 7.4-Å cryo-EM structure of an EF-G-bound ribosome stalled by the addition of the antibiotics fusidic acid and viomycin [20]. Viomycin stabilizes the pre-translocation tRNA in the decoding center [20,83] without inhibiting GTP hydrolysis [84,85]. The low resolution prevented a detailed structural analysis of the GTPase center in the antibiotic-bound structure. To further resolve the GTPase center in the pre-translocation EF-G state, we used cryo-EM to visualize a pre-translocation 70S complex assembled with EF-G•GTP and viomycin (Fig. S2). Remarkably similar to Structure III, the 3.2-Å resolution structure of the viomycin-stalled ribosome (i.e., III-vio; Fig. S2d) features a better resolved GTPase center (Figs. 4b,f and S3i). Structure III-vio supports our finding that the pre-translocation ribosome contains post-hydrolysis Pi and GDP (Fig. 4b) stabilized by the switch loops and ions, likely magnesium [29,86], which coordinate the phosphate groups (Fig. 4f). Thus, our structures reveal that (a) GTP is hydrolyzed on pre-translocation ribosome, and (b) after hydrolysis, the switch loops of the GTPase center remain well ordered because they are stabilized by the rotated 30S conformation.

Structure IV, by contrast, features a post-Pi-release conformation of EF-G. Here, movement of EF-G into the 30S A site coincides with separation of the GTPase domain from the SRL (Fig. 4d). The GTP-binding pocket is ~2 Å further from the catalytic SRL phosphate than in Structure III, consistent with an inactive post-reaction state (Fig. S6k). The GTPase movement relative to the SRL is consistent with mutational studies showing that perturbing the conformation of the SRL abolishes translocation even if the GTPase activity is retained [74]. Whereas GDP is clearly

resolved, densities for the switch loops and Pi are absent (Figs. 4c-d and S3k), indicating that the switch loops become dynamic and thus release Pi from the GTPase center [81,87]. These rearrangements of EF-G coincide with a >10-Å movement of h14 away from sw-I, as a result of reverse 30S rotation (Fig. 4d). Thus, disruption of the contact between the 30S and GTPase is correlated with Pi release.

Structural mechanism of EF-G•GTP-catalyzed translocation

Time-resolved cryo-EM of authentic translocation answers several long-standing questions; rationalizes previous structural, biochemical and biophysical observations; and suggests a parsimonious model for the translocation mechanism (Fig. 5 and Supplementary Video 1). As Structures I through II-C report, pre-translocation ribosomes spontaneously interconvert between non-rotated and rotated conformations, in which the peptidyl-tRNA samples A/A, A/P and A/P* states (Fig. 5a-d). This is consistent with a large body of biochemical and biophysical data reporting fast tRNA fluctuations on the 50S subunit and intersubunit rotation prior to EF-G binding [8,15,88-90]. EF-G•GTP binds to a rotated pre-translocation ribosome [32], where the relative position of the small subunit and the 50S SRL are complementary to the GTP-bound conformation of EF-G's GTPase domain, as in Structure III (Fig. 5e,k). The EF-G translocase domain 4 binds near the ASL of the A/P* tRNA (Fig. 5e). Because EF-G is sterically incompatible with A/A and A/P tRNA conformations (Fig. S5e-f), this binding must shift the conformational equilibrium toward the "elbow-translocated" A/P* conformation. Indeed, in the 25-second dataset with EF-G, no classes of rotated ribosomes with the A/P and A/A tRNA (as in Structures II-A and II-B) are observed, indicating substantial depletion in comparison with the 0-second dataset (Figs. 1c and S1). Binding of EF-G to the rotated pre-translocation ribosome is consistent with biochemical observations of transient stabilization of the rotated 70S by EF-G with GTP or GTP analogs and increased rates of forward 30S rotation [10,82].

Structures of EF-G-bound intermediates (III through V) report the trajectory of translocation consistent with FRET solution studies showing that translocation on the 30S subunit occurs during the reverse 30S rotation [19] and proceeds in at least two steps [7,91]. During spontaneous reverse rotation of the 30S subunit, EF-G domain 4 sterically hinders the A/P* tRNA from returning to the canonical A/A state (Figs. S5e-f and S6f-h). The tip of domain 4 initially wedges between the tRNA and the shoulder of the 30S subunit (Structure III) and then enters the A site, separating, or "unlocking", the tRNA from the decoding center in Structure IV. Loops 1 and 2 of domain 4 interact with the tRNA and with the 30S head (Fig. 3a-b), in keeping with their critical role in tRNA unlocking and 30S head swivel required for translocation [92]. Reverse 30S rotation moves EF-G into the A site first by ~20 Å (from Structure III to IV) and then by ~4 Å (from Structure IV to V), completing translocation relative to the 30S body. The transition of EF-G relative to the A site is consistent with those observed in solution studies [93]. Moreover, EF-G and ribosome rearrangements closely resemble eEF2 and eukaryotic ribosome transitions inferred from a cryo-EM study of IRES translocation [60]. Thus, the conserved elongation factors induce unlocking and retain contact with peptidyl-tRNA to bias the diffusion of tRNA-mRNA along the mRNA tunnel from the A to P site.

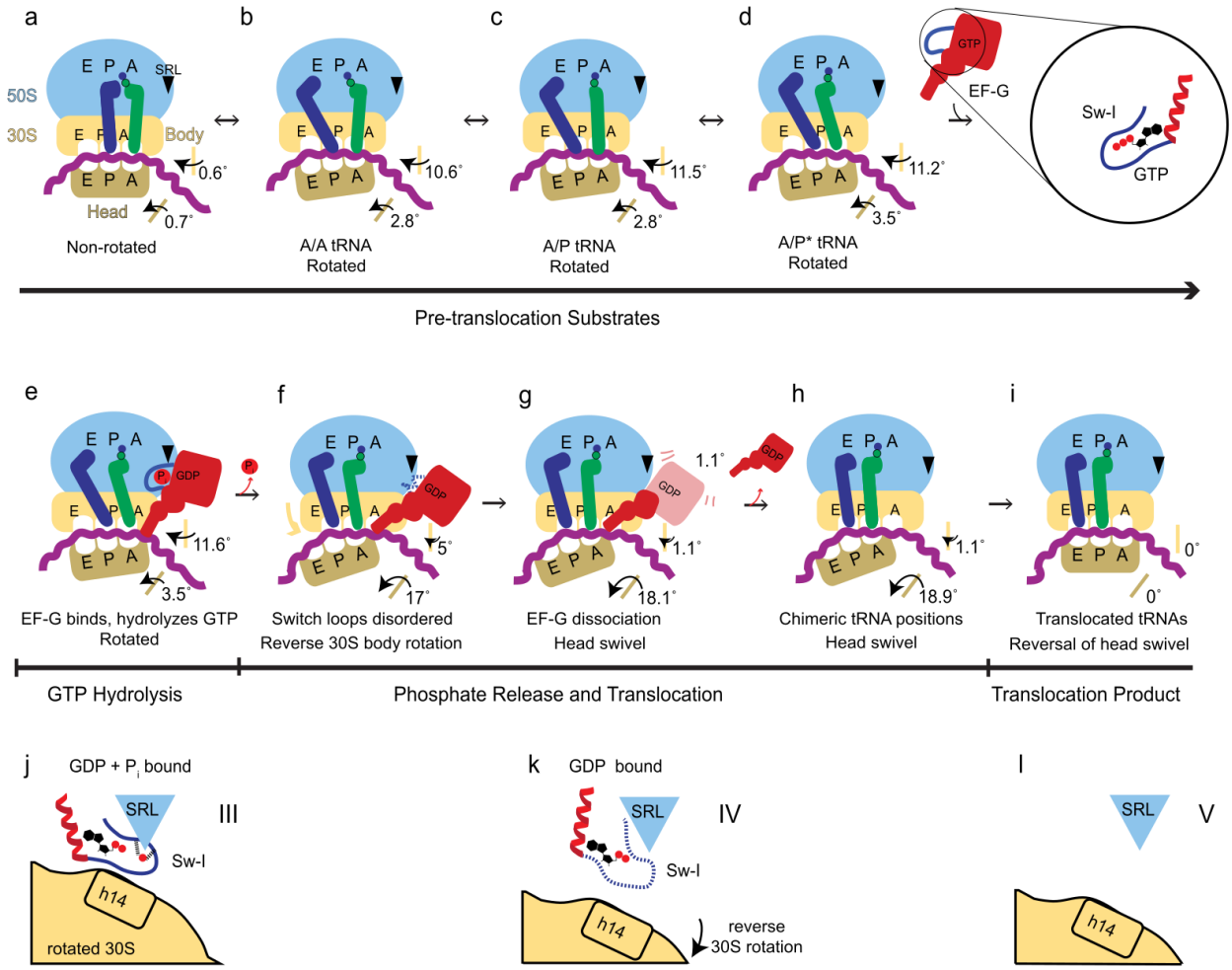

Figure 5. Schematic of ribosomal translocation catalyzed by EF-G and GTP. a-i, Progression of translocation and rearrangements of ribosomal subunits, EF-G and tRNAs. **j-l**, Rearrangement of EF-G GTPase switch loop I, showing the coupling of Pi release with 30S rotation and translocation.

Consistent with FRET studies, the structural intermediates with extensive ~20˚ head swivel (IV and V), occur on-pathway [7,61] to retain the interactions between the 30S head and translocating tRNAs. Novel states in the 25-s dataset with the most translocated tRNAs and most swiveled 30S head capture a transient equilibrium between the ribosomes with EF-G (Structure V) and without EF-G (Structure VI), suggesting that EF-G•GDP can dissociate from ribosomes prior to the reversal of head swivel (Fig. S4g-h). Despite extensive classification, our data has not revealed EF-G bound to non-rotated/non-swiveled ribosomes, suggesting that they are exceedingly rare if they exist during authentic translocation. By contrast, non-rotated/non-swiveled ribosomes with EF-G were reported when EF-G cannot dissociate due to the inability to hydrolyze GTP or due to the presence of an antibiotic [24,25,28]. Our findings therefore illustrate that EF-G•GTP-catalyzed translocation of tRNAs occurs in two major steps: first, relative to the 30S body, coincident with the forward head swivel (with EF-G); second, relative to the head, upon reversal of the head swivel (without EF-G, or coincident with EF-G dissociation).

Our work provides structural insights into the role of GTP hydrolysis in translocation. EF-G accelerates translocation by more than 3 orders of magnitude with either GTP or non-hydrolyzable GTP analogs [39,43,45]. Yet, translocation rates are 2- to 50-fold higher with GTP than with GTP analogs [19,33,39,46] or with inactivating His92 mutations [25,47]. The structural basis for this difference has remained unclear. Our structures demonstrate that rather than being coupled with the chemical step of GTP hydrolysis, tRNA translocation is coupled with switch-loop rearrangements of EF-G and phosphate release (from Structure III to Structure IV). Structures III and III-vio are consistent with biochemical studies, showing that Pi release is slower than hydrolysis and may determine the rate of tRNA translocation [44,80,81]. In the pre-translocation ribosome (Structure III), sw-I bridges the SRL with the rotated 30S subunit, preserving an ordered GTP-bound-like conformation of EF-G GTPase. Reversal of the 30S subunit rearranges sw-I, allowing Pi diffusion from the GTPase center (Structure III to IV). By contrast, artificially preventing the release of Pi—e.g., in the presence of non-hydrolyzable GTP analogs or catalytically defective EF-G mutants—stabilizes a GTP-bound-like conformation of EF-G until late translocation states [25,28]. The inability of sw-I to rearrange correlates with the reduced rates of reverse 30S rotation with GTP analogs [19], at least in part explaining the slower translocation. Moreover, in the presence of non-hydrolyzable GTP analogs, the GTP-like conformation of EF-G prevents dissociation of the GTPase domain from the SRL at latter stages of translocation [25,28], which coincide with the reversal of head swivel (Structure IV to V to VI). Our structural analyses of EF-G-bound intermediates (Structures III through V) highlight that GTP hydrolysis contributes to the directionality and completion of translocation by enabling a stepwise loss of EF-G contact with the ribosome (Fig. 3f). Indeed, single-molecule FRET and biochemical studies showed that transitions between the late translocation states [7] and dissociation of EF-G [44] may determine the rates of EF-G•GTP-catalyzed translocation.

Due to the strict directionality, large-scale tRNA movements, and fast rates of GTP-catalyzed translocation, some mechanistic models proposed that translocation is driven by large-scale rearrangements of EF-G [26,36-38]. Discussions considered that EF-G could act as a flexible GTPase motor, akin to classic ATP-driven motors [94], such as myosin and kinesin, whose conformational changes are commensurate with their molecular size [95-98]. The structures captured in this work suggest that EF-G does not act as a highly flexible motor and that the proposed nearly 100-Å rearrangement of domain 4 [26] (Fig. S7d) is not required for translocation to occur (see *Supplementary discussion*). EF-G adopts similarly extended conformations in the pre-translocation state before Pi release (Structure III) and in the nearly post-translocated ribosome after Pi release (Structure IV). The ~7 Å displacement of domain 4 from the GTPase domain (Fig. 3c) cannot account for ~25-Å translocation of tRNA and mRNA. Rather, the EF-G interdomain movement is consistent with spontaneous thermal fluctuations of ~10 Å observed in solution studies [67], inferred from the changes in FRET efficiencies [99]. Thus, modest interdomain rearrangement of EF-G accounts for accommodation of domain 4 in the 30S A site during reverse 30S rotation. If some large-scale interdomain EF-G rearrangements occur on the ribosome [36], they must take place prior to formation of the pre-translocation Structure III and thus do not drive translocation. By contrast, the 30S body rotation [8,12] and head swivel [57,100-102] are the inherent and spontaneously sampled properties of the ribosome, which have been observed without EF-G. The

rates of intersubunit rotation are directly coupled to the rates of translocation [19,103], indicating that ribosomal rearrangements are the driver of translocation. Thus, EF-G accelerates translocation by acting as a nearly-rigid steric block (i.e., a pawl), that rectifies inherent ribosomal rearrangements into tRNA movement on the 30S subunit. The GTPase activity serves as a switch controlling the ability of EF-G to bind and leave the ribosome (Fig. 5j-i).

The translocation intermediates captured in this work also illustrate how the mRNA frame is preserved to prevent frameshifting events that could produce toxic proteins and premature termination. While the pre-translocation ribosome stabilizes the tRNA-mRNA helix in the decoding center [63,64,66] and in the P-site [48,56,104], the thermodynamically labile three-basepair codon-anticodon helix may be destabilized during the transition between these two sites, leading to tRNA slippage and frameshifting [28,105,106]. Indeed, recent crystal structure revealed that the tRNA-mRNA base-pairing can be destabilized in the absence of EF-G, if the 30S head is swiveled similarly to that in our Structure V [101]. We have also recently obtained cryo-EM structures of ribosomes with a frameshifting-prone mRNA, which suggest that +1 frameshifting can occur before completion of the 30S head swivel [28]. In the current work, Structures IV and V feature domain 4 of EF-G interacting with both the codon and the anticodon (Fig. S6f-h). They demonstrate that EF-G must remain bound to the ribosome until achieving the latest head-swiveled intermediate Structure V with the most translocated tRNAs, to support the tRNA-mRNA helix and prevent frameshifting.

Together with recent cryo-EM studies of translation initiation [107,108], mRNA decoding [53,64,65], termination [109-111] and recycling [112], our work offers a more complete structural visualization of the ribosomal translation cycle. Consistent with biochemical studies, the structural studies revealed that similar inherent and spontaneous ribosomal dynamics (e.g., intersubunit rotation, 30S head swivel) are essential for each step of translation, and that translation factors provide checkpoints that promote accuracy and directionality. These structural dynamics are similar between bacterial systems (*E. coli* and *Th. thermophilus* being the predominant model systems), yeast and mammalian cytosolic and mitochondrial ribosomes, in keeping with the central role of ribosomal RNA and universal conservation of the two-subunit and subunit-domain architecture of the ribosome [113-116].

Supplementary Discussion

Large-scale interdomain rearrangements of EF-G are unlikely to drive translocation

Mechanistic models involving large-scale interdomain EF-G dynamics of up to 100 Å at least in part rely on the crystallographic structure that reports a 70S ribosome with a highly compact EF-G•GDP [26]. Domain 4 in that structure is shifted by nearly 100 Å from its position in our Structures and in numerous ribosome structures that capture extended EF-G in the presence of inhibitors (Fig. S7). The compact EF-G was stalled on a pre-translocation-like non-rotated ribosome (similar to Structure I), using a non-productive aminoacyl-tRNA analog and EF-G mutant fused to ribosomal protein L9 of the crystallographically-related neighboring ribosome [26]. Extensive classification of non-rotated ribosomes in our 25-s dataset, including masks focused on the compact EF-G conformation, has not revealed a similar state. Although a minor population of ribosomes with compact EF-G might be below the limit of detection in our data, we note the compact crystallographic conformation appears incompatible with binding of EF-G with GTP. Indeed, formation of the 70S complex with L9-EF-G was only possible in the presence of GDP, whereas GTP prevented L9-EF-G from binding the ribosome [26]. In both free and ribosome-bound EF-G or EF-G homologs, domain 3 stabilizes sw-I in the presence of GTP or GTP analogs [25,28,69]. This GTP-compatible conformation sharply contrasts the compact L9-EF-G [26], in which domain 3 is shifted by 35 Å away from the GTPase center (Fig. S7d). Furthermore, the compact EF-G places its GTPase domain ~4 Å away from its catalytic position near the SRL, incompatible with GTP hydrolysis. Finally, the area of contact between compact EF-G and the ribosome (~2500 Å^2) is much lower than that in Structure III (3730 Å^2). This indicates a less favorable affinity of compact EF-G to the non-rotated ribosome than that of extended EF-G to the rotated ribosome, in keeping with biochemical data [32]. Nevertheless, even if transient large-scale EF-G rearrangements occur on the ribosome [36], they must take place prior to formation of the pre-translocation Structure III and thus do not drive translocation.

Methods

Preparation of EF-G and ribosomal subunits

The gene encoding the full-length C-terminally His_6-tagged *E. coli* EF-G was cloned into a pET24a+ vector (Novagen, kanamycin resistance), and the plasmid was transformed into *E. coli* BLR/DE3 cells. The cells were cultured in Luria-Bertani (LB) medium with 50 μg mL^{-1} kanamycin at 37°C until the OD_{600} of 0.7-0.8. Expression of EF-G was induced by 1 mM IPTG (Gold Biotechnology Inc., USA), followed by cell growth for 9 hrs at 16°C. The cells were harvested, washed and resuspended in buffer A: 50 mM Tris•HCl pH=7.5, 50 mM NH_4Cl, 10 mM $MgCl_2$, 5% glycerol, 10 mM imidazole, 6 mM β-mercaptoethanol (βME) and protease inhibitor (complete Mini, EDTA-free protease inhibitor tablets, Sigma Aldrich, USA). The cells were disrupted with a microfluidizer (Microfluidics, USA), and the soluble fraction was collected by centrifugation at 18,000 rpm for 50 minutes and filtered through a 0.22 μm pore size sterile filter (CELLTREAT Scientific Products, USA).

EF-G was purified in three steps. The purity of the protein after each step was assessed by 12% SDS-PAGE stained with Coomassie Brilliant Blue R 250 (Sigma-Aldrich). First, affinity chromatography with Ni-NTA column (Nickel-nitrilotriacetic acid, 5 ml HisTrap, GE Healthcare) was performed using FPLC (Äkta explorer, GE Healthcare) at 4°C. The cytoplasmic fraction was loaded onto the column equilibrated with buffer A and washed with the same buffer. EF-G was eluted with a linear gradient of buffer B (buffer A with 0.25 M imidazole). Fractions containing EF-G were pooled and dialyzed against buffer C (50mM Tris•HCl pH=7.5, 100 mM KCl, 10 mM $MgCl_2$, 0.5 mM EDTA, 6 mM βME and protease inhibitor). The second purification step involved ion-exchange chromatography using a 20ml HiPrep FF Q-column (GE Healthcare). The column was equilibrated and washed with buffer C. EF-G sample was loaded in buffer C and eluted with a linear gradient of buffer D (buffer C with 0.7 M KCl). Finally, the protein was dialyzed against 50 mM Tris•HCl pH=7.5, 100 mM KCl, 10 mM $MgCl_2$, 0.5 mM EDTA, 6 mM βME, and purified using size-exclusion chromatography (Hiload 16/600 Superdex 200pg column, GE Healthcare). The fractions of the protein were pulled, buffer-exchanged (25 mM Tris•HCl pH=7.5, 100 mM NH_4Cl, 10 mM $MgCl_2$, 0.5 mM EDTA and 6 mM βME, 5% glycerol) and concentrated with an ultrafiltration unit using a 10-kDa cutoff membrane (Millipore). The concentrated protein was flash-frozen in liquid nitrogen and stored at -80°C.

70S ribosomes were prepared from *E. coli* (MRE600) as described [117,118], and stored in the ribosome-storage buffer (20 mM Tris•HCl (pH 7.0), 100 mM NH_4Cl, 12.5 mM $MgCl_2$, 0.5 mM EDTA, 6 mM βME) at -80°C. Ribosomal 30S and 50S subunits were purified using sucrose gradient (10-35%) in a ribosome-dissociation buffer (20 mM Tris•HCl (pH 7.0), 500 mM NH_4Cl, 1.5 mM $MgCl_2$, 0.5mM EDTA, 6 mM βME). The fractions containing 30S and 50S subunits were collected separately, concentrated and stored in the ribosome-storage buffer at -80°C.

Preparation of charged tRNAs and mRNA

Native *E. coli* $tRNA^{fMet}$ was purchased from Chemical Block and was aminoacylated as described (Lancaster and Noller, 2005). Native *E. coli* $tRNA^{Pro}$ (UGG) was over-expressed in *E. coli* from an IPTG-inducible *proM* gene encoded by the pKK223-3 plasmid. Total tRNA was isolated using differential centrifugation [119], and $tRNA^{Pro}$(UGG) was isolated using a complementary biotinylated oligonucleotide attached to streptavidin-sepharose [120], yielding approximately 40 nmoles $tRNA^{Pro}$(UGG) from 1 liter of culture. $tRNA^{Pro}$ (UGG) (10 μM) was aminoacylated in the charging buffer (50 mM Hepes pH 7.5, 50 mM KCl, 10 mM $MgCl_2$, 10 mM DTT) in the presence of 40 μM L-proline, 2 μM prolyl-tRNA synthetase, 0.625 mM ATP and 15 μM elongation factor EF-Tu. EF-Tu was purified as described [64]. The mixture was incubated for 10 minutes at 37°C. To stabilize the charged Pro-$tRNA^{Pro}$ in the form of Pro-$tRNA^{Pro}$•EF-Tu•GTP ternary complex, 0.25 mM GTP was added to the mixture. The mixture was incubated for 3 minutes at 37°C.

Model mRNA, containing the Shine-Dalgarno sequence and a linker to place the AUG start codon in the P site (GGC AAG GAG GUA AAA AUG **CCA A**GU UCU AAA AAA AAA AAA) was synthesized by IDT.

Preparation of the 70S translocation complex with EF-G•GTP

The 70S•mRNA•fMet-$tRNA^{fMet}$•Pro-$tRNA^{Pro}$•EF-G•GTP reactions were prepared as follows. First, a pre-translocation complex with $tRNA^{Pro}$ in the A site was assembled. 0.33 μM 30S subunit (all concentrations are specified for the final solution) were pre-activated at 42°C for 5 minutes in the ribosome-reconstitution buffer (20 mM HEPES pH 7.5, 120 mM NH_4Cl, 20 mM $MgCl_2$, 2 mM spermidine, 0.05 mM spermine, 6 mM βME). 0.33 μM 50S subunit with 1.33 μM mRNA were added to the 30S solution and incubated for 10 minutes at 37°C. To form the 70S initiation-like complex, 0.33 μM fMet-$tRNA^{fMet}$ was added, and the solution was incubated for 3 minutes at 37°C. To deliver Pro-$tRNA^{Pro}$ to the A site, the pre-incubated ternary complex (Pro-$tRNA^{Pro}$ at 0.33 μM; EF-Tu at 0.5 μM; GTP at 0.25 mM) was added to the solution and incubated for 10 minutes at 37°C, as described [28].

Translocation complexes with EF-G were formed by addition of the mixture of ice-cooled 5.3 μM EF-G and 0.66 mM GTP to the ice-cooled pre-translocation complex, on ice. No EF-G and GTP were added to the 0-second time point reaction, which was applied to a grid and blotted as described below. The 10-μL reaction with EF-G was mixed and an aliquot was immediately applied on the grid, blotted and plunged into a cryogen, as described below, resulting in the 25-second time-point sample. The 3600-second sample was obtained by incubation of the pre-translocation complex with EF-G and GTP for 60 minutes on ice followed by grid blotting and plunging.

To form a viomycin-bound pre-translocation complex (Structure III-vio), 0.13 mM viomycin was added to the pre-translocation complex and incubated for 3 minutes at 37°C. 5.3 μM EF-G and 0.66 mM GTP were added to the solution, incubated for 5 minutes at 37°C, cooled down to room temperature, applied to a grid and plunged into a cryogen.

Cryo-EM grid preparation, data collection and image processing

QUANTIFOIL R 2/1 grids with 2nm carbon layer (Cu 200, Quantifoil Micro Tools) were glow discharged with 25 mA with negative polarity for 60 seconds in a PELCO easiGlow glow discharge unit. 2.5 µl of each complex separately was applied to the grids. Grids were blotted at blotting force 10 for 4 seconds at 5°C, 95% humidity, and plunged into liquid ethane using a Vitrobot MK4 (FEI). Grids were stored in liquid nitrogen.

Data collection and processing of all datasets were performed similarly to those for the 25-second data set (Fig. S1 and Table S1), with differences outlined below. Cryo-EM data were collected at the Cryo-EM Center, University of Massachusetts Medical School. From a grid with the 70S•mRNA•fMet-tRNA^{fMet}•Pro-tRNA^{Pro} complex that was cryogen-plunged 25 seconds after mixing with EF-G•GTP, 4943 movies were collected on a Titan Krios microscope operating at 300 kV (FEI/ThermoFisher) equipped with a K3 Summit camera system (Gatan), with the defocus range of -0.8 to -2.0 µm. Multi-shot multi-hole data acquisition was performed by recording four shots per grid hole from four holes at a time [109], using SerialEM [121] with beam-image shift. Each exposure was acquired with continuous frame streaming at 33 frames per 1.977 s yielding a total dose of 47.58 $e^-/Å^2$. The dose rate was 16.54 e^-/pixel/s at the camera. The nominal magnification was 105,000 and the calibrated super-resolution pixel size at the specimen level was 0.415 Å. The movies were motion-corrected, and frame averages were calculated using all frames within each movie, after multiplying by the corresponding gain reference in IMOD [122]. During motion-correction, the movies were binned to the pixel size of 0.83 Å (termed unbinned or 1× binned). cisTEM [123] was used to determine defocus values for each frame average and to pick ribosome particles. 238 movies with large drift, low signal, heavy ice contamination, or very thin ice were excluded from further analysis after inspection of the averages and the power spectra computed by CTFFIND4 within cisTEM. The stack of 475,746 particles and particle parameter files were assembled in cisTEM with the binnings of 1×, 2×, 4×, and 8× and the box size of 448 unbinned $pixel^3$. FREALIGNX was used for particle alignment, refinement and final reconstruction steps. FREALIGN v9.11 was used for 3D classification steps [124], as shown in Fig. S1. The 8x-binned image stack was initially aligned to a 70S ribosome reference (PDB 5U9F) [125] using 5 cycles of mode 3 alignment (global search), including data in the resolution range of 300-30 Å until the convergence of the average score. Subsequently, the 8× binned stack was aligned against the common reference resulting from the previous step, using mode 1 (refine) in the resolution range 300-18 Å (3 cycles of mode 1). The 2× binned image stack was then aligned against the common reference using mode 1 (refine) in several steps, in which the high-resolution limits gradually increased to 8 Å (5 cycles per each resolution limit). 3D density reconstruction was obtained using 60% particles with the highest scores. Subsequently, the refined particle parameters were used for classification of the 2× binned stack into 16 classes in 100 cycles, using the resolution range of 300-8 Å. This classification revealed 9 high-resolution classes, 4 low-resolution (junk) classes, and 3 classes representing only 50S subunit (Fig. S1a). The particles assigned to the high-resolution classes were extracted from the 2× binned stack (with > 50% occupancy and > 0 score) using merge_classes.exe (part of FREALIGN distribution), resulting in the stack of 262,085 particles. Classification of this stack was performed for 100 cycles using a spherical mask (40 Å

radius) focused to cover most of the ribosomal A and P sites. Classification into 16 classes yielded two 70S maps, each of which contained densities for two tRNAs and EF-G. To better resolve the positions of tRNAs and EF-G, these maps were subject to additional classification. To this end, the particles assigned to these two classes were extracted from the 2× binned stack into two sub-stacks (with > 50% occupancy and scores > 0) using merge_classes.exe, resulting in stack-1 and stack-2 with 7,173, and 12,327 particles, respectively. Prior to classification, stack-1 was re-refined, as described above, using the high-resolution cutoff of 6 Å. Classification was performed for 100 cycles, using the same A site focused mask. Classification yielded into 2 classes yielded a 3.3 Å class (Structure IV) which contained both tRNAs and EF-G, and a class containing a rotated ribosome with P/E tRNA. An additional classification of stack-1 using a separate masking strategy was performed (Fig. S1b). Classification of stack-1 was performed for 100 cycles, using a focused spherical mask with the radius of 35 Å, covering the GTPase domain of EF-G. Classification into 2 classes yielded a 3.3 Å class (Structure IV_{gtpase}) which contained both tRNAs and EF-G, and a heterogenous class requiring further classification. Subsequent classification of the second class into 2 classes using a focused mask of 30 Å around the 50S E site produced a 3.9 Å class with two tRNAs and EF-G (Structure V), and a heterogenous class requiring additional classification. A final classification of the heterogenous class for 100 cycles with a 35-Å spherical focused mask around the translocase domain of EF-G produced a 3.8 Å class that contained the 70S ribosome with a swiveled head, two tRNAs, and no EF-G (Structure VI). Stack-2 exhibited heterogeneity at the EF-G binding site and 30S domain conformation, so it was first classified into 2 classes for 100 cycles, using a 3D mask covering the shoulder domain, filtered to 30 Å and down-weighted to 0.1. The class containing EF-G was used to create a substack of 5,379 particles (stack-2a) which was subjected to a 100-cycle classification into 3 classes using the original 40 Å A site mask. This classification produced a 3.8 Å class of 1,657 particles containing a pre-translocation 70S•2tRNA•EFG state (Structure III). An additional classification of stack-2a using a separate masking strategy was performed (Fig. S1c). Classification of stack-2a was performed for 100 cycles, using a focused spherical mask with the radius of 35 Å, covering the GTPase domain of EF-G. Classification into 3 classes yielded a 3.7 Å class of 1,884 particles containing a pre-translocation 70S•2tRNA•EFG state (Structure III_{gtpase}).

Data collection and processing for the 0-second time point pre-translocation 70S•mRNA•fMet-$tRNA^{fMet}$•Pro-$tRNA^{Pro}$ complex were performed as follows. 1161 movies were collected on the Titan Krios microscope described above, with the -0.5 to -1.5 µm defocus range. Multi-shot multi-hole data acquisition was performed using SerialEM as described above. Each exposure was acquired with continuous frame streaming at 25 frames per 0.999 s yielding a total dose of 40.12 $e^-/Å^2$. The movies were motion-corrected and frame averages were calculated using all frames in IMOD. The nominal magnification was 82,000 and the calibrated super-resolution pixel size at the specimen level was 0.415 Å. During motion-correction, the movies were binned to the pixel size of 0.83 Å (termed unbinned or 1× binned). The initial alignment, refinement and 3D classification of the stack of 137,421 particles into 16 classes for 100 cycles was performed, as described for the 25-second dataset above, with the exception of an *ab initio* model generated

from 50% of the particles was used for initial alignment. After excluding the low-resolution (junk) classes and classes representing the 50S subunit, the extracted particles were combined into a 2×-binned substack (91,638 particles) and classified into 16 classes using a 40-Å focused spherical mask placed between the A and P sites (as in the 25-second data set) to resolve the pre-translocation classes. Seven classes containing non-rotated pre-translocation ribosomes were combined (37,252 particles) and refined resulting in Structure I. Three classes with rotated ribosomes were merged to create stack-1 (14,890-particles) and 5 classes of rotated ribosomes were merged to create stack-2 (24,819 particles) for further classification. With the same 40 Å mask, the stack-1 was classified into 5 classes for 100 cycles. Structure II-B and II-C were reconstructed at 1x for a final resolution of 4.2 Å and 4.3 Å, respectively. Second subclassification approach resulted in Structure II-A. Stack-2 was classified into 12 classes using a 40 Å slightly shifted so that the center was in line with the A-site finger of the 50S subunit. The classification was run for 500 cycles and Structure II-A was reconstructed at 1x from a single class at a final resolution of 3.8 Å.

2,574 movies were collected for the 3600-second 70S•mRNA•fMet-tRNA^{fMet}•Pro-tRNA^{Pro}•EF-G•GTP complex on a Talos Arctica microscope operating at 200 kV (FEI), equipped with a K3 Summit camera system (Gatan), with the defocus range of -0.5 to -1.5 µm. Multi-shot data collection was performed by recording shots from four holes at a time, using SerialEM, as described above. Each exposure was acquired with continuous frame streaming at 27 frames per 1.13 s, yielding a total dose of 30.4 e^-/Å^2. The dose rate was 16.48 e^-/pixel/s at the camera. The movies were motion-corrected and frame averages were calculated using all frames within each movie after multiplying by the corresponding gain reference in IMOD. The nominal magnification for the dataset was 45,000 and the calibrated super-resolution pixel size at the specimen level was 0.435 Å. During motion-correction, the movies were binned to the pixel size of 0.87 Å. The initial alignment, refinement and 3D classification of the original 170,799-particle stack into 16 classes were performed as described for the 25-second dataset. After excluding the low-resolution classes and classes representing the 50S subunit, the extracted particles were combined into a 2x-binned substack (132,070 particles) and classified into 16 classes using a 40-Å focused spherical mask positioned between the A and P sites, as in the 0- and 25-second data sets. Post-translocation states were combined into a single stack of 55,457 particles and refined using a 6 Å resolution cutoff, resulting in the 2.9 Å map (Structure VII).

For the viomycin-bound 70S•mRNA•fMet-tRNA^{fMet}•Pro-tRNA^{Pro}•EF-G•GTP pre-translocation complex, a dataset of 4740 movies was collected on a Talos Arctica microscope operating at 200 kV (FEI) equipped with a K3 Summit camera system (Gatan), with the defocus range of -0.5 to -1.5 µm. Multi-shot data collection was performed by recording shots from four holes at a time, using SerialEM, as described above. Each exposure was acquired with continuous frame streaming at 27 frames per 1.618 s yielding a total dose of 30.48 e^-/Å^2. The dose rate was 14.30 e^-/pixel/s at the camera. The nominal magnification was 45,000 and the calibrated super-resolution pixel size at the specimen level was 0.435 Å. The movies were motion-corrected and frame averages were calculated using all frames within each movie after multiplying by the corresponding gain reference in IMOD. During motion-correction in IMOD the movies were binned

to pixel size 0.87 Å (termed unbinned or 1× binned). cisTEM was used to determine defocus values for each frame average and for particle picking. 114 movies with large drift, low signal, heavy ice contamination, or very thin ice were excluded from further analysis after inspection of the averages and the power spectra computed by CTFFIND4 within cisTEM. The stack of 517,847 particles and the particle parameter files were assembled in cisTEM with the binnings of 1×, 2×, 4×, and 8× and the box size of 448 unbinned pixel. Particle alignment and refinement against the the 8×-binned and 2×-binned stacks were performed as described for the 25-second dataset. The 2× binned stack was classified into 16 classes in 50 cycles, using the resolution range of 300-8 Å. This classification revealed 9 high-resolution classes, 5 low-resolution (junk) classes and 2 classes representing the 50S subunit (Fig. S2). Particles assigned to the high-resolution classes were extracted from the 2× binned stack (with > 50% occupancy and scores > 0) using merge_classes.exe (part of the FREALIGN distribution), and merged into a stack containing 322,549 particles. Classification of this stack was performed for 50 cycles using a focused spherical mask with the 30-Å radius, covering most of the A and P sites. Classification into 16 classes yielded 3 high-resolution classes, each of which contained two tRNAs and EF-G. The particles assigned to the 3 high-resolution classes were extracted from the 2× binned stack (with > 50% occupancy and scores > 0) using merge_classes.exe (part of the FREALIGN distribution), and merged into a stack containing 48,345 particles. Classification of this stack was performed for 50 cycles using a focused spherical mask at the A site (30 Å radius, as implemented in FREALIGN). Classification into 3 classes yielded a single high-resolution class, which contained two tRNAs and EF-G. Additional classification of each class into more classes did not yield additional high-resolution structures with EF-G. For the class of interest (Structure III-vio, 20,167 particles), particles with > 50% occupancy and scores > 0 were extracted from the 2× binned stack. Refinement to 6 Å resolution using mode 1 (5 cycles) of the 1× binned stack using 95% of particles with highest scores resulted in a 3.4 Å map (FSC=0.143). Beamtilt correction to the Nyquist limit (beamtilt(x,y)mrad = -0.0198 -0.0290 ; particle shift x,y (A) = 0.0849, 0.1189) has further improved map quality, yielding a 3.2 Å map (FSC=0.143).

Local-resolution filtering was applied to the resulting cryo-EM maps by a previously optimized procedure [53], using blocres and blocfilt from the Bsoft package [126], followed by sharpening the blocfiltered maps with bfactor.exe using a constant B-factor of −50 Å^2 to the average resolution determined by FSC_part. These maps were used for model building and structure refinements. Maps sharpened or softened with different B-factors (from -125 to +50 Å^2) were also used to interpret high-resolution details or lower-resolution features. FSC curves were calculated by FREALIGN for even and odd particle half-sets (Figs. S1-2).

Model building and refinement

Cryo-EM structure of *E. coli* 70S•fMet-tRNA^{Met}•Phe-tRNA^{Phe}•EF-Tu•GDPCP Structure III [64], excluding EF-Tu and tRNAs, was used as a starting model for structure refinements. The structures of EF-G were created by homology modeling and map fitting, using ribosome-bound EF-G structures including PDB 4V7D (Brilot et al. 2013, PNAS), PDB 7K51, PDB 4V9H [27], PDB 4W29 [21] and the crystal structure of EF-G-2 (PDB 1WDT) as references. Initial protein and

ribosome domain fitting into cryo-EM maps was performed using Chimera [127], followed by manual modeling using Pymol [128]. The linkers between the domains and parts of the domains that were not well defined in the cryo-EM maps (e.g. ribosomal proteins or loops of EF-G) were not modeled.

Atomic models were refined against corresponding cryo-EM maps by real-space simulated-annealing refinement using atomic electron scattering factors in RSRef [129,130] as described [55]. Secondary-structure restraints, comprising hydrogen-bonding restraints for ribosomal proteins and base-pairing restraints for RNA molecules, were employed as described [131]. Refinement parameters, such as the relative weighting of stereochemical restraints and experimental energy term, were optimized to produce stereochemically optimal models that closely agree with the corresponding maps. In the final stage, the structures were refined using phenix.real_space_refine [132], followed by a round of refinement in RSRef applying harmonic restraints to preserve protein backbone geometry and atomic B-factor refinement in phenix.real_space_refine. The refined structural models closely agree with the corresponding maps, as indicated by low real-space R-factors of ~0.25 and Correlation Coefficients of ~0.75 (Table S1) and visual inspection of the models and maps. The resulting models have excellent stereochemical parameters as indicated by the low MolProbity scores of ~2, low deviations from ideal bond lengths and angles, low number of protein and RNA outliers and other structure-quality statistics (Table S1). Structure quality was validated using MolProbity [133].

Structure superpositions and distance calculations were performed in Pymol. To calculate an angle of the 30S body or head rotation with respect to Structure VII, 23S rRNA (body rotation) or the 16S rRNA excluding the head domain (i.e. residues 2–920 and 1398–1540; head rotation) were aligned with the corresponding rRNA from Structure VII using PyMOL, and the angles between 16S body or head regions were measured in Chimera. Figures were prepared in PyMOL and Chimera [127,128]. Buried surface area (contact area) for EF-G domains was calculated in Pymol using the refined EF-G structures (III, IV and V) with generated hydrogen atoms in the presence and absence of the ribosome components.

ACKNOWLEDGEMENTS

We thank Chen Xu and Kangkang Song for grid screening and data collection at the cryo-EM facility at UMass Medical School; Darryl Conte Jr. and members of the Korostelev laboratory for discussions and comments on the manuscript. This study was supported by LL2008 project, MEYS CR as a part of the ERC CZ program and by Czech Science Foundation, project no. 20-16013Y (to G.D.), and by NIH Grants F31 HL152650 (to C.E.C.), R35 GM134931 (to Y.M.H.) and R35 GM127094 (to A.A.K.).

AUTHOR CONTRIBUTIONS

Conceptualization: G.D., A.A.K. Methodology: C.E.C., G.D., A.B.L., H.G., Y.M.H., A.A.K. Validation: C.E.C, G.D., A.A.K. Investigation: C.E.C., G.D. Resources: Y.M.H., G.D., A.A.K. Writing- Original Draft: C.E.C., A.A.K. Writing- Review and Editing: All; Visualization: C.E.C., A.B.L., G.D., A.A.K. Supervision: A.A.K. Funding Acquisition: C.E.C., Y.M.H, G.D., A.A.K.

COMPETING INTERESTS: Authors declare no competing interests.

Supplementary Table 1. Cryo-EM data collection and structure refinement statistics.

	I	II-A	II-B	II-C	III	III-vio	IV	V	VI	VII
Data collection and processing										
Magnification	82,000 x	82,000 x	82,000 x	82,000 x	105,000 x	45,000x	105,000 x	105,000 x	105,000 x	45,000x
Voltage (kV)	300	300	300	300	300	200	300	300	300	200
Electron exposure (e–/Å^2)	40.12	40.12	40.12	40.12	47.6	30.5	47.6	47.6	47.6	30.4
Defocus range (μm)	-0.5-1.5	-0.5-1.5	-0.5-1.5	-0.5-1.5	-0.8-2.0	-0.5-1.5	-0.8-2.0	-0.8-2.0	-0.8-2.0	-0.5-1.5
Pixel size (Å)	0.83	0.83	0.83	0.83	0.8271	0.87	0.8271	0.8271	0.8271	0.87
Symmetry imposed	C1	C1	C1	C1	C1	C1	C1	C1	C1	C1
Initial particle (no.)	137,421	137,421	137,421	137,421	475,746	517,847	475,746	475,746	475,746	170,799
Final particle (no.)	37,252	3,026	2,108	1,963	1,657	20,167	3,778	1,105	1,163	55,457
Map resolution (Å)**	3.0	3.8	4.2	4.3	3.8	3.2	3.26	3.9	3.8	2.9
FSC threshold	0.143	0.143	0.143	0.143	0.143	0.143	0.143	0.143	0.143	0.143
Map resolution range (Å)	2.5-4	3.5-6	3.5-6	3.5-6	3.0-6	3.0-4.5	3.0-6	3.0-6	3.0-6	2.5 -3.5
Refinement										
Initial model used (PDB code)	5UYM	5UYM	5UYM	5UYM	5UYM	5UYM	5UYM	5UYM	5UYM	5UYM
Model resolution (Å)	3.0	3.8	4.2	4.3	3.8	3.2	3.26	3.9	3.8	2.9
Correlation Coefficient (cc_mask)*	0.80	0.71	0.69	0.81	0.73	0.82	0.74	0.72	0.72	0.87
Real space R-factor †	0.22	0.27	0.25	0.24	0.28	0.21	0.26	0.27	0.28	0.19
Map sharpening *B* factor (Å^2)	0	-50	+25	+100	-65	0	-50	-50	-50	0
Model composition*										
Non-hydrogen atoms	150,712	147,013	148,629	149,100	154,533 6,781	154,581 6,781	154,332 6,753	151,339 6,370	149,126 6,084	149,037 6,084
Protein residues	6,083	6,091	6,025	6,084	4,735	4,735	4,736	4,736	4,736	4,732
RNA residues	4,811	4,635	4,735	4,735						
B factors (Å^2)*										
Protein	141.53	124.41	281.93	406.07	140.45	156.77	107.13	154.16	127.73	144.26
RNA	144.02	126.79	273.07	417.08	115.79	136.93	108.82	152.99	123.76	137.87
R.m.s. deviations*,§										
Bond lengths (Å)	0.008	0.008	0.009	0.008	0.015	0.007	0.007	0.011	0.010	0.011
Bond angles (°)	1.1	1.1	1.1	1.0	1.1	1.0	1.1	1.2	1.1	1.3
Validation*										
MolProbity score	2.39	2.52	2.39	2.30	2.29	2.13	2.33	2.74	2.48	2.02
Clashscore	10.90	12.99	13.36	14.72	11.82	9.68	10.33	19.00	18.97	11.67
Poor rotamers (%)	1.83	1.63	1.39	0.67	1.52	1.01	1.54	2.06	0.85	0.40
Ramachandran plot*										
Favored (%)	86.25	79.93	85.50	86.62	89.26	87.39	85.53	80.83	82.16	93.31
Allowed (%)	13.75	18.22	14.13	13.38	10.02	11.32	12.75	18.63	17.84	6.69
Disallowed (%)	0.00	1.86	0.37	0.00	0.72	1.29	1.72	0.54	0.00	0.00
Validation (RNA)*										
Good sugar pucker (%)	99.3	99.7	99.6	99.8	99.6	99.7	99.4	99.5	99.4	98.1
Good backbone (%)#	82.3	81.6	84.5	83.6	82.5	83.5	82.3	78.3	77.5	79.1

** from Frealign (FSC_part)
* from Phenix
† from RSRef
§ root mean square deviations
# RNA backbone suites that fall into recognized rotamer conformations defined by Molprobity

Supplementary Table 2. Conformations of the 30S subunit (body rotation and head swivel) and EF-G in 70S translocation structures with 2 tRNAs and EF-G from this work and previous studies with antibiotics, EF-G mutation or GTP analogs.

Structure (method; reference; PDB code)	**Formed with EF-G and:**	**[#] Body rotation; Head swivel (°)**	**tRNA conformations**	**EF-G conformation** (GTP, GTPase center)
Structures I – VII (this work; cryo-EM)				
I	**GTP**	0.6; 0.7	A/A and P/P	No EF-G
II-A		10.6; 2.8	A/A and P/E	No EF-G
II-B		11.5; 2.8	A/P and P/E	No EF-G
II-C		11.2; 3.5	A/P* and P/E	No EF-G
III		11.6; 3.5	A/P* and P/E	Ordered switch loops, **GDP and Pi** resolved (or, less likely GTP) near SRL
IV		5.0; 17.0	ap/P and pe/E	Disordered switch loops, **GDP near SRL** (slightly shifted away, relative to Structure III)
V		1.1; 18.1	ap*/P and pe*/E	Density for GTPase domain 1 and domain 2 is absent, domain 3 weak.
VI		1.1; 18.9	ap*/P and pe*/E	No EF-G
VII		0; 0	P/P and E/E	No EF-G
Structures of 70S•2tRNA•EF-G complexes captured with inhibitors and/or mutations				
Pre-translocation-like:				
7.6 Å cryo-EM, *E. coli*; Brilot et al, 2013; PDB 4V7D	Vio, Fus, **GTP**	12.1; 3.4	A/P* and P/E	Ordered GTPase near SRL; insufficient resolution.
2.9 Å cryo-EM, *E. coli* (**this work**)	Vio, **GTP**	12.2; 3.4	A/P* and P/E	Ordered switch loops, **GDP and Pi**
2.8 Å X-ray; *T. thermophilus*; Lin et al, 2015); PDB 4WPO	**GDP** (L9-EF-G fusion, non-hydrolyzable aminoacyl-tRNA analogs)	2.3; 1.5	A/A and P/P	Compact EF-G, domain 3 shifted away from GTPase; GTPase ~10 Å from SRL; switch loops disordered; **GDP**
Mid-translocation-like (swiveled head)				

6.8 Å cryo-EM, *E. coli*; Ramrath et al. 2013; PDB 4V7B	Fus and GTP	5.1; 16.4	ap/P and pe/E	Disordered switch loops
3.8 Å X-ray, *T. thermophilus*; Zhou et al, 2014; PDB 4W29	Fus, Neomycin and GTP	4.6; 18.7	ap/ap and pe/E	Disordered switch loops, Fus, **GDP**
3.5 Å cryo-EM, *E. coli;* (Structure II in Demo et al, 2020); PDB 7K51	**GDPCP**	5.7; 15.8	ap/P and pe/E	Ordered switch loops, **GDPCP**
Post-translocation-like (nearly non-rotated)				
3.6 Å cryo-EM; *E. coli*; Li et al, 2015; PDB 3J9Z	H91A EF-G mutant, **GTP**	0.4; 1.0	P/P and E/E	Ordered switch, GTP
3.6 Å X-ray; *T. thermophilus*; Gao et al, 2009; PDB 4V5F	Fus and **GDP**	2.6; 1.3	P/P and E/E	Disordered switch loops, Fus, **GDP**
3.4 Å cryo-EM, *E. coli;* (Structure III in Demo et al, 2020); PDB 7K52	**GDPCP**	2.5; 2.1	P/P and E/E	Ordered switch loops, **GDPCP**

[#] 30S body rotation and head swivel are measured relative to the non-rotated post-translocation Structure VII.

Supplementary Figures

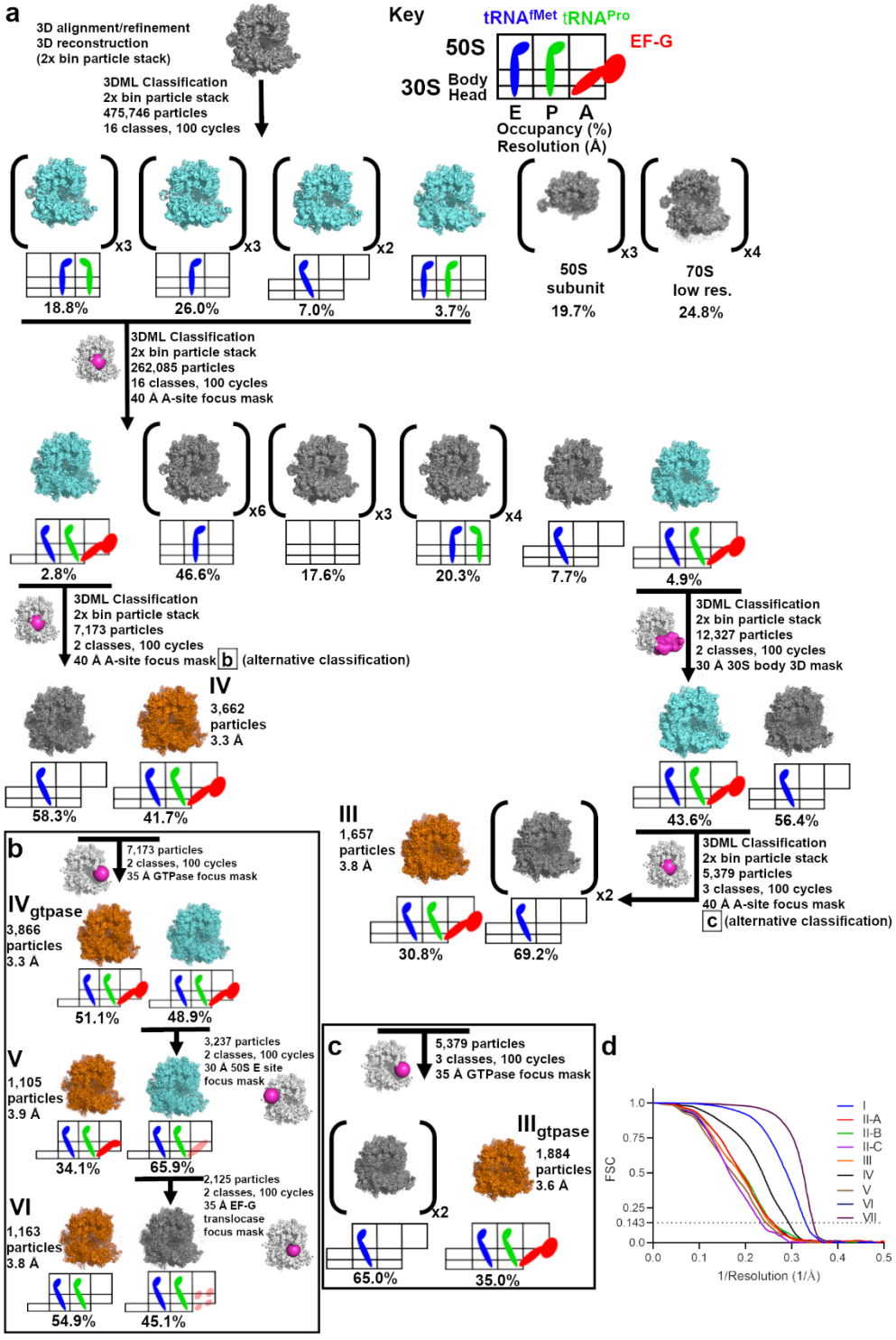

Supplementary Fig. 1. Scheme of maximum-likelihood classification of the 25-second data set resulting in Structures III to VI. a, Classification scheme and key showing tRNA and EF-G binding sites on the ribosome. **b-c,** Alternative classification schemes. **d,** FSC between even- and odd-particle half maps for each Structure in 0-s, 25-s, and 3600-s data sets.

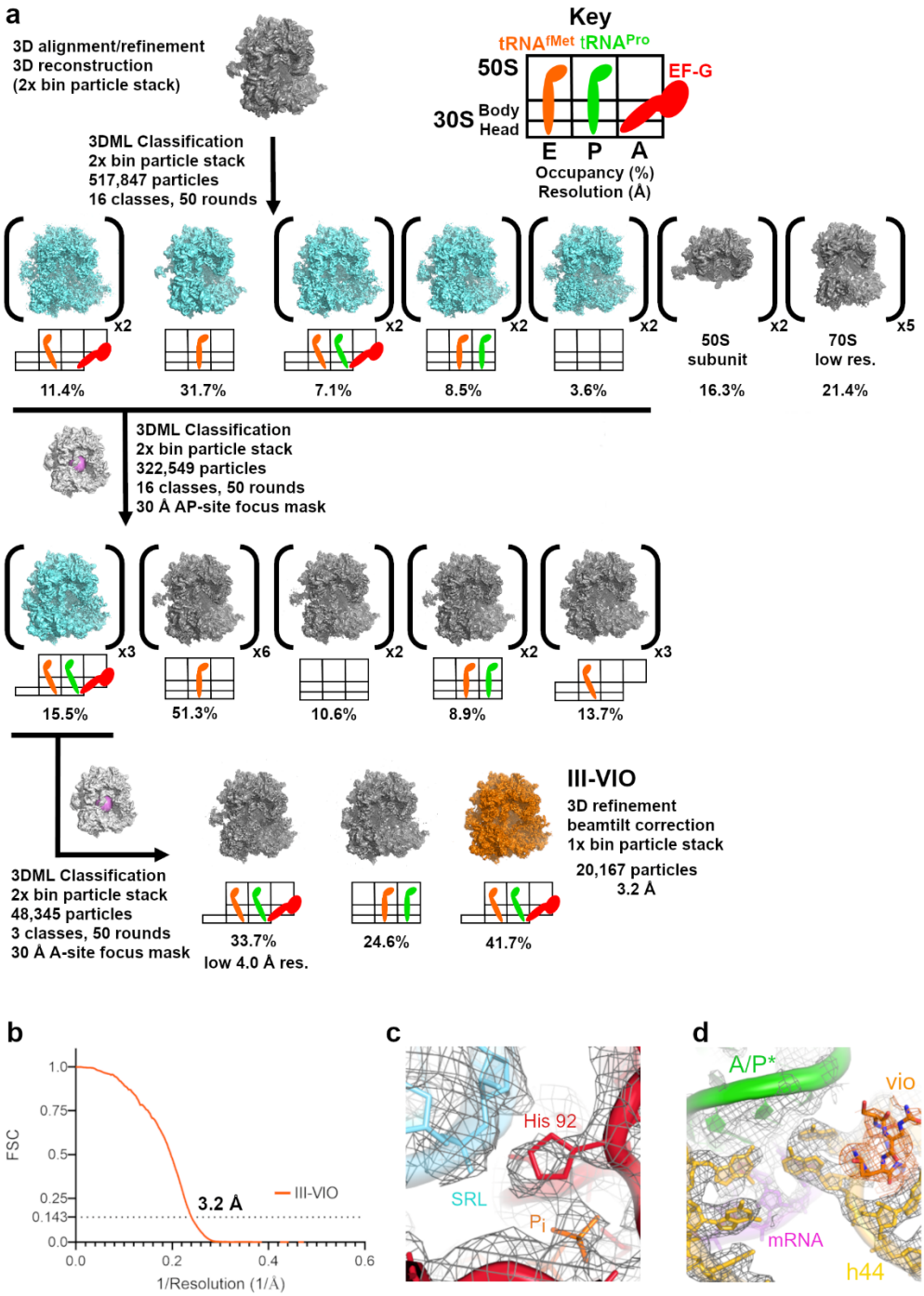

Supplementary Fig. 2. Scheme of maximum-likelihood classification of the data set resulting in Structure III-vio. a, Classification scheme and key showing tRNA and EF-G binding sites on the ribosome. **b,** FSC between even- and odd-particle half maps for Structure III-vio. **c-d,** Close-up views of cryo-EM density (mesh) for the GTPase center of EF-G near SRL (**c**) and the decoding center of the 30S subunit bound with viomycin (**d**).

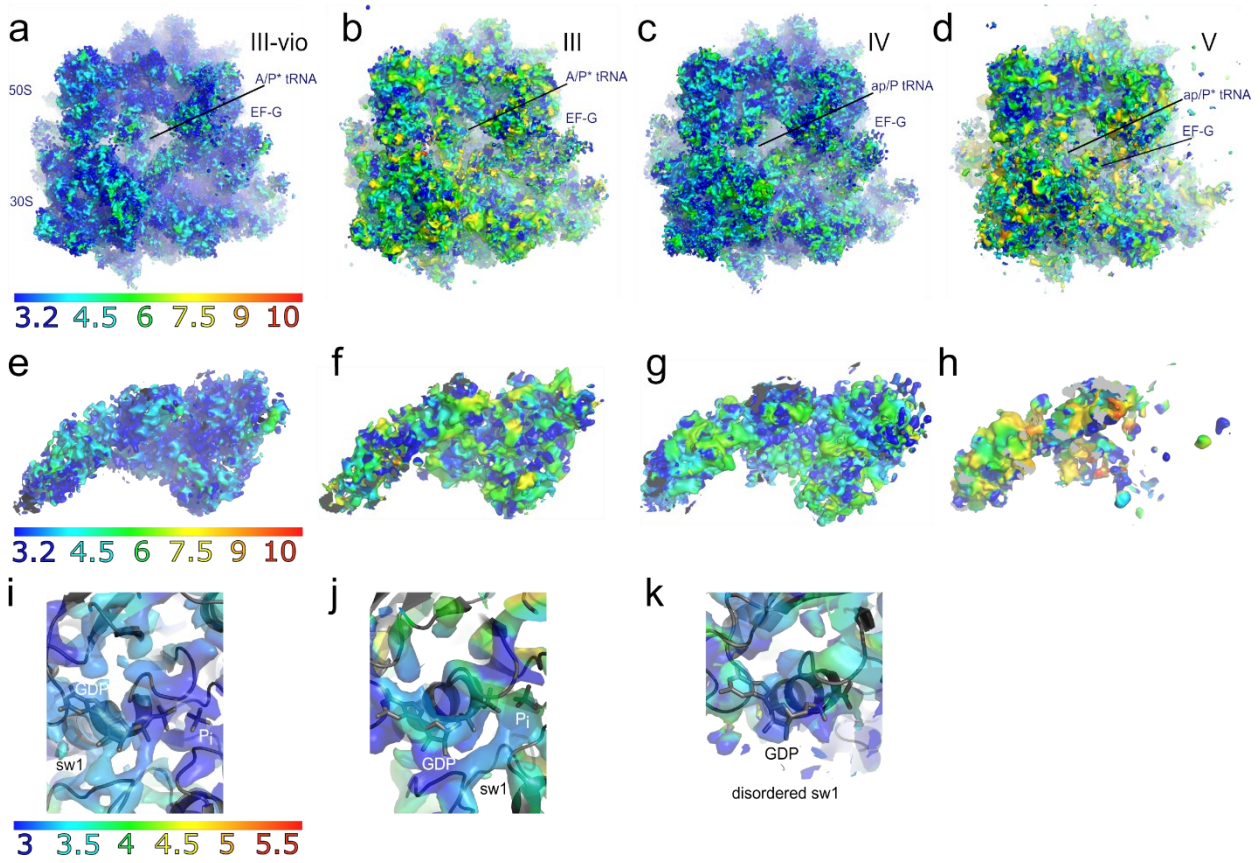

Supplementary Fig. 3. **Local resolutions for the EF-G-bound Structures III-vio, III, IV and V). a,** An overview of the Structure III-vio map. The sharpened map (B-factor= -50) is shown at 2.25σ, coloured using a local-resolution scale ranging from 3.2 Å to 10 Å. **b-d,** Overviews of Structures III through V. The sharpened maps (III B-factor = -65; IV B-factor = -50; V B-factor = -50) are shown at 2.25σ, coloured using a local-resolution scale ranging from 3.2 Å to 10 Å. **e-h,** Local resolution of EF-G density in Structures III-vio, III, IV and V. **i-k**, Close-up views of local resolutions of the GTPase center of EF-G in Structures III-vio, IV and V. Local resolution of the maps was assessed using blocres and blocfilt from the Bsoft package, as described in Methods.

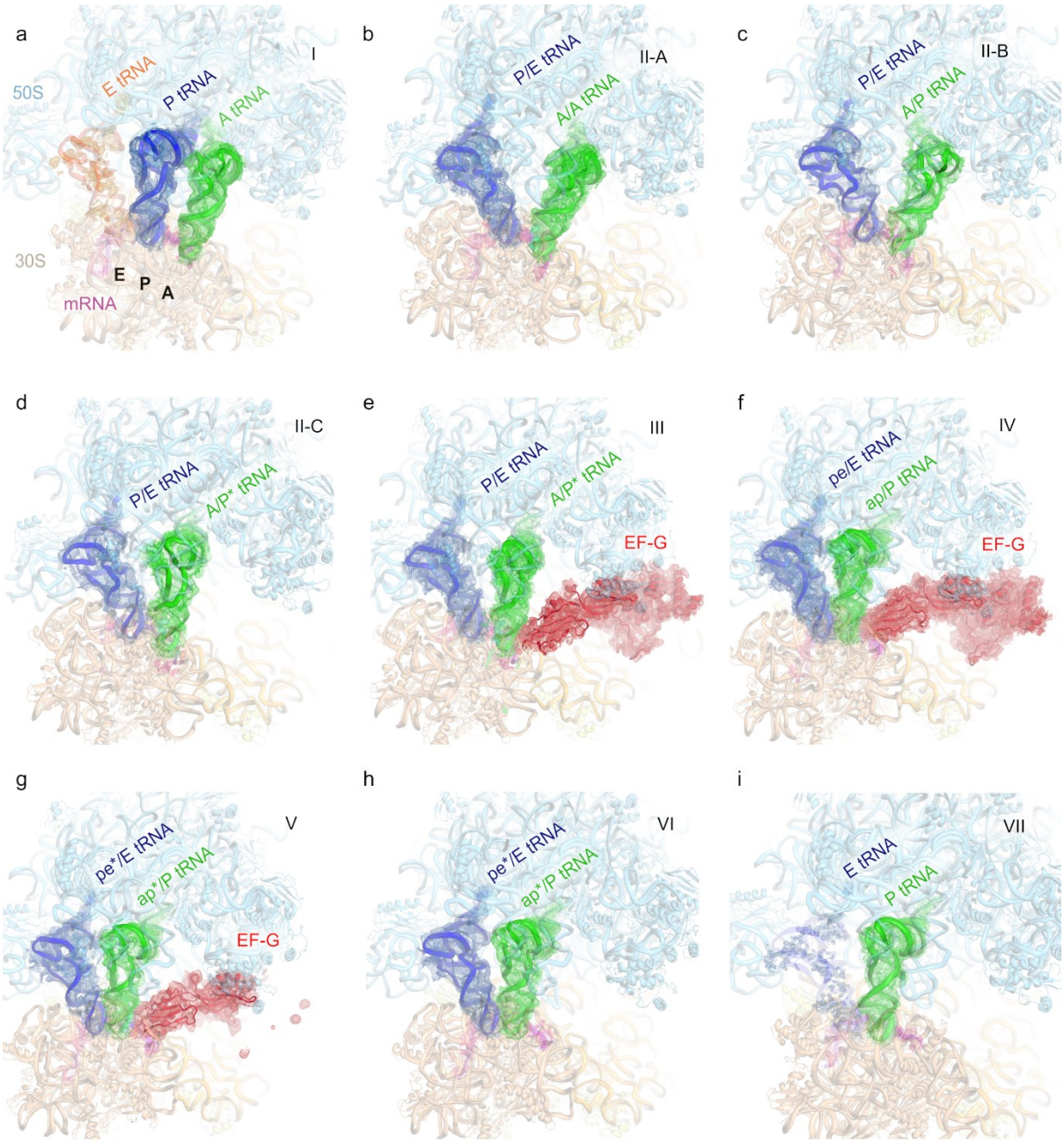

Supplementary Fig. 4. **Cryo-EM densities (mesh) for tRNAs and EF-G in Structures I through VII.** All tRNA and EF-G densities are set to the same sigma within each panel.

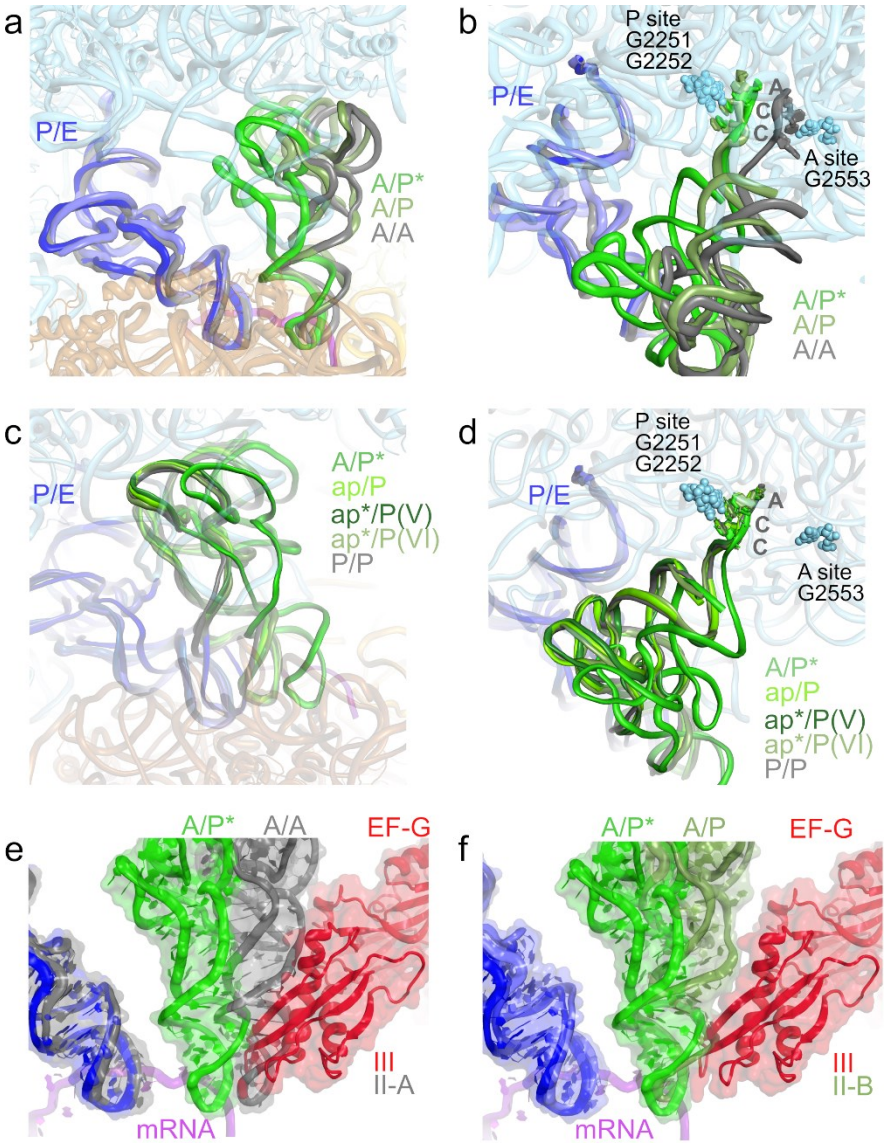

Supplementary Fig. 5. **Positions and conformations of A/A, A/P and A/P* tRNA in Structures II-A, II-B, and II-C, respectively. a.,** Alignment of Structures II-A, II-B, and II-C show how the A tRNA advances towards the 50S P site. P/E tRNA from all three structures (grey, slate, blue) is shown for reference. **b.,** The CCA end of A/A tRNA resides in the 50S A site (G2553) while the CCA end of A/P and A/P* tRNA resides in the 50S P site (G2251-2252). **c.,** Alignment of Structures III, IV, V, VI, and VII show that $tRNA^{Pro}$ occupies the 50S P site. P/E tRNA from all structures except VII (blue, deep blue, sky blue, slate) is shown for reference. **d.,** The CCA end of $tRNA^{Pro}$ resides in the 50S P site (G2251-2252) for all five structures. **e-f.,** EF-G domain 4 clashes with A/A (grey) and A/P tRNA (smudge green).

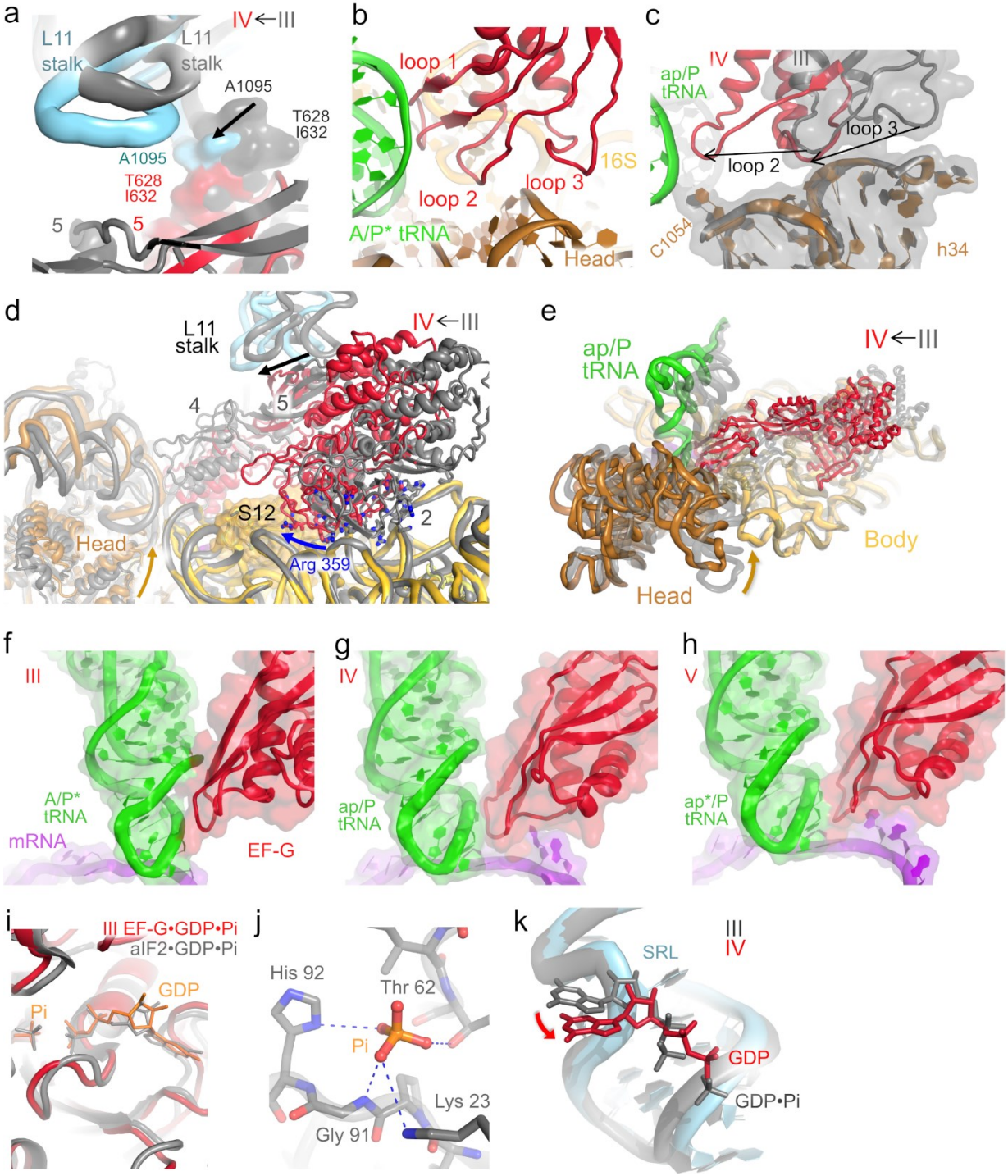

Supplementary Fig. 6. **Comparison of EF-G in Structures III and IV. a,** Alignment on 23S rRNA shows L11 residue 1095 packing on EF-G residues 628 and 632 in Structure III and IV. **b,** Interactions of the three loops at the tip of EF-G domain 4 with the ribosomal rRNA and tRNA in Structure III **c,** Loops 2 and 3 of EF-G domain 4 change positions to interact with the same region of the 30S head domain in Structures III and IV, respectively. **d,** Positively charged residues of EF-G domains 2 and 3 (shown as sticks) slide along 16S rRNA toward S12, from Structure III to

IV. **e,** Comparison of the positions of the translocating dipeptidyl-tRNA, EF-G and 30S head in Structures III (gray) and IV (colored, as specified by the labels). Structures III and IV were superimposed by the structural alignment of the 30S body domain (all rRNA nucleotides except for 921-1397); ribosomal proteins are omitted for clarity. **f-h,** EF-G directly contacts the ASL throughout translocation **i,** Conformation of the GTPase center of EF-G in Structure III is similar to those in free translational GTPases bound with GTP: a crystal structure of an archaeal initiation factor aIF2•GTP is shown for comparison (gray; PDB 4RD1 [86]). **j,** Coordination environment for the putative phosphate ion includes positively charged residues and hydrogen bonding donors (within 3.5 Å from the putative oxygen positions). **k,** Alignment on 23S rRNA shows that GDP moves ~2 Å away from the SRL between structures III and IV.

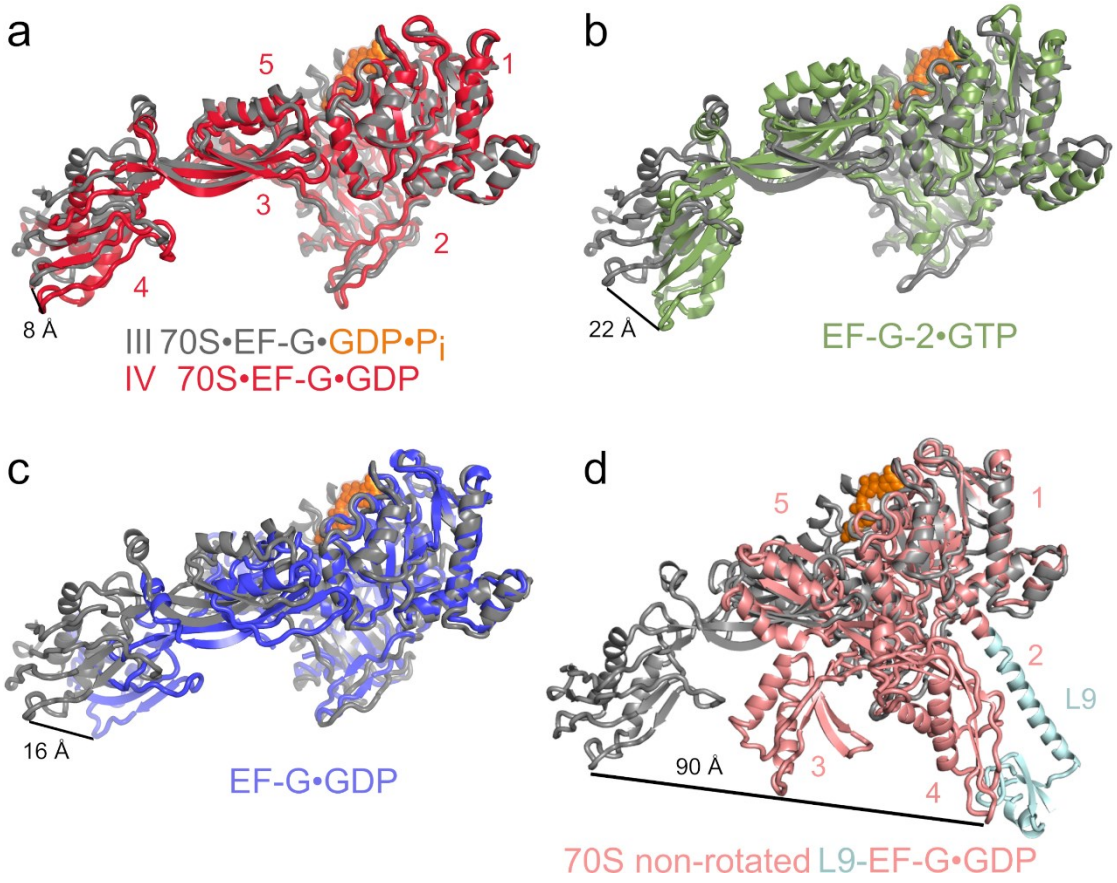

Supplementary Fig. 7. **Comparison of the position of EF-G domain 4 in the pre-translocation Structure III (gray with orange GDP*Pi) and in other structures of free and ribosome-bound EF-G and EF-G homologs. a,** EF-G•GDP in Structure IV (red); **b,** crystal structure of *T. thermophilus* EF-G-2 with GTP (green; PDB 2DY1 [69]); **c,** crystal structure of *T. thermophilus* EF-G (blue; PDB 2EFG [62]); **d,** compact *T. thermophilus* L9-EF-G•GDP fusion protein crystallized in the non-rotated 70S ribosome (pink; PDB 4WPO [26]). Domains of EF-G (1-5) are labeled in panels a and d. Superposition was performed by structural alignment of domains 1-2s. The distance between the tips of domain 4 (at *E. coli* aa 511) is shown.

Supplementary Video 1. Animation showing tRNA and mRNA translocation by EF-G•GTP. Two scenes demonstrate how translocation is coupled with conformational changes of the small 30S subunit: 1) 30S body rotation, and 2) 30S head swivel.

REFERENCES

1 Ling, C. & Ermolenko, D. N. Structural insights into ribosome translocation. *WIREs RNA*, (2016).

2 Noller, H. F., Lancaster, L., Zhou, J. & Mohan, S. The ribosome moves: RNA mechanics and translocation. *Nat Struct Mol Biol* **24**, 1021-1027, (2017).

3 Rodnina, M. V. Translation in Prokaryotes. *Cold Spring Harb Perspect Biol* **10**, (2018).

4 Voorhees, R. M. & Ramakrishnan, V. Structural basis of the translational elongation cycle. *Annu Rev Biochem* **82**, 203-236, (2013).

5 Chen, J., Tsai, A., O'Leary, S. E., Petrov, A. & Puglisi, J. D. Unraveling the dynamics of ribosome translocation. *Curr Opin Struct Biol* **22**, 804-814, (2012).

6 Frank, J. & Gonzalez, R. L., Jr. Structure and dynamics of a processive Brownian motor: the translating ribosome. *Annu Rev Biochem* **79**, 381-412, (2010).

7 Wasserman, M. R., Alejo, J. L., Altman, R. B. & Blanchard, S. C. Multiperspective smFRET reveals rate-determining late intermediates of ribosomal translocation. *Nat Struct Mol Biol* **23**, 333-341, (2016).

8 Cornish, P. V., Ermolenko, D. N., Noller, H. F. & Ha, T. Spontaneous intersubunit rotation in single ribosomes. *Mol Cell* **30**, 578-588, (2008).

9 Sternberg, S. H., Fei, J., Prywes, N., McGrath, K. A. & Gonzalez, R. L., Jr. Translation factors direct intrinsic ribosome dynamics during translation termination and ribosome recycling. *Nat Struct Mol Biol* **16**, 861-868, (2009).

10 Sharma, H. *et al.* Kinetics of Spontaneous and EF-G-Accelerated Rotation of Ribosomal Subunits. *Cell Rep* **16**, 2187-2196, (2016).

11 Valle, M. *et al.* Locking and unlocking of ribosomal motions. *Cell* **114**, 123-134, (2003).

12 Frank, J. & Agrawal, R. K. A ratchet-like inter-subunit reorganization of the ribosome during translocation. *Nature* **406**, 318-322, (2000).

13 Fischer, N., Konevega, A. L., Wintermeyer, W., Rodnina, M. V. & Stark, H. Ribosome dynamics and tRNA movement by time-resolved electron cryomicroscopy. *Nature* **466**, 329-333, (2010).

14 Agirrezabala, X. *et al.* Visualization of the hybrid state of tRNA binding promoted by spontaneous ratcheting of the ribosome. *Mol Cell* **32**, 190-197, (2008).

15 Munro, J. B., Altman, R. B., O'Connor, N. & Blanchard, S. C. Identification of two distinct hybrid state intermediates on the ribosome. *Mol Cell* **25**, 505-517, (2007).

16 Blanchard, S. C., Kim, H. D., Gonzalez, R. L., Jr., Puglisi, J. D. & Chu, S. tRNA dynamics on the ribosome during translation. *Proc Natl Acad Sci U S A* **101**, 12893-12898, (2004).

17 Bretscher, M. S. Translocation in protein synthesis: a hybrid structure model. *Nature* **218**, 675-677, (1968).

18 Moazed, D. & Noller, H. F. Intermediate states in the movement of transfer RNA in the ribosome. *Nature* **342**, 142-148, (1989).

19 Ermolenko, D. N. & Noller, H. F. mRNA translocation occurs during the second step of ribosomal intersubunit rotation. *Nat Struct Mol Biol* **18**, 457-462, (2011).

20 Brilot, A. F., Korostelev, A. A., Ermolenko, D. N. & Grigorieff, N. Structure of the ribosome with elongation factor G trapped in the pretranslocation state. *Proc Natl Acad Sci U S A*, (2013).

21 Zhou, J., Lancaster, L., Donohue, J. P. & Noller, H. F. How the ribosome hands the A-site tRNA to the P site during EF-G-catalyzed translocation. *Science* **345**, 1188-1191, (2014).

22 Zhou, J., Lancaster, L., Donohue, J. P. & Noller, H. F. Crystal structures of EF-G-ribosome complexes trapped in intermediate states of translocation. *Science* **340**, 1236086, (2013).

23 Ramrath, D. J. *et al.* Visualization of two transfer RNAs trapped in transit during elongation factor G-mediated translocation. *Proc Natl Acad Sci U S A* **110**, 20964-20969, (2013).

24 Gao, Y. G. *et al.* The structure of the ribosome with elongation factor G trapped in the posttranslocational state. *Science* **326**, 694-699, (2009).

25 Li, W. *et al.* Activation of GTP hydrolysis in mRNA-tRNA translocation by elongation factor G. *Sci Adv* **1**, (2015).

26 Lin, J., Gagnon, M. G., Bulkley, D. & Steitz, T. A. Conformational changes of elongation factor G on the ribosome during tRNA translocation. *Cell* **160**, 219-227, (2015).

27 Tourigny, D. S., Fernandez, I. S., Kelley, A. C. & Ramakrishnan, V. Elongation factor G bound to the ribosome in an intermediate state of translocation. *Science* **340**, 1235490, (2013).

28 Demo, G. *et al.* Structural basis for +1 ribosomal frameshifting during EF-G-catalyzed translocation. *BioRxiv*, (2020).

29 Pulk, A. & Cate, J. H. Control of ribosomal subunit rotation by elongation factor G. *Science* **340**, 1235970, (2013).

30 Holtkamp, W. *et al.* GTP hydrolysis by EF-G synchronizes tRNA movement on small and large ribosomal subunits. *EMBO J* **33**, 1073-1085, (2014).

31 Wilden, B., Savelsbergh, A., Rodnina, M. V. & Wintermeyer, W. Role and timing of GTP binding and hydrolysis during EF-G-dependent tRNA translocation on the ribosome. *Proc Natl Acad Sci U S A* **103**, 13670-13675, (2006).

32 Hauryliuk, V. *et al.* The pre-translocation ribosome is targeted by GTP-bound EF-G in partially activated form. *Proc. Natl. Acad. Sci. U S A*, (in press), (2008).

33 Chen, J., Petrov, A., Tsai, A., O'Leary, S. E. & Puglisi, J. D. Coordinated conformational and compositional dynamics drive ribosome translocation. *Nat Struct Mol Biol* **20**, 718-727, (2013).

34 Rodnina, M. V., Peske, F., Peng, B. Z., Belardinelli, R. & Wintermeyer, W. Converting GTP hydrolysis into motion: versatile translational elongation factor G. *Biol Chem* **401**, 131-142, (2019).

35 Peske, F., Matassova, N. B., Savelsbergh, A., Rodnina, M. V. & Wintermeyer, W. Conformationally restricted elongation factor G retains GTPase activity but is inactive in translocation on the ribosome. *Mol Cell* **6**, 501-505, (2000).

36 Chen, C. *et al.* Elongation factor G initiates translocation through a power stroke. *Proc Natl Acad Sci U S A* **113**, 7515-7520, (2016).

37 Yin, H., Gavriliuc, M., Lin, R., Xu, S. & Wang, Y. Modulation and Visualization of EF-G Power Stroke During Ribosomal Translocation. *Chembiochem* **20**, 2927-2935, (2019).

38 Yao, L., Li, Y., Tsai, T. W., Xu, S. & Wang, Y. Noninvasive measurement of the mechanical force generated by motor protein EF-G during ribosome translocation. *Angew Chem Int Ed Engl* **52**, 14041-14044, (2013).

39 Rodnina, M. V., Savelsbergh, A., Katunin, V. I. & Wintermeyer, W. Hydrolysis of GTP by elongation factor G drives tRNA movement on the ribosome. *Nature* **385**, 37-41, (1997).

40 Desai, V. P. *et al.* Co-temporal Force and Fluorescence Measurements Reveal a Ribosomal Gear Shift Mechanism of Translation Regulation by Structured mRNAs. *Mol Cell* **75**, 1007-1019 e1005, (2019).

41 Liu, T. *et al.* Direct measurement of the mechanical work during translocation by the ribosome. *Elife* **3**, e03406, (2014).

42 Kaziro, Y. The role of guanosine 5'-triphosphate in polypeptide chain elongation. *Biochim Biophys Acta* **505**, 95-127, (1978).

43 Gavrilova, L. P., Kostiashkina, O. E., Koteliansky, V. E., Rutkevitch, N. M. & Spirin, A. S. Factor-free ("non-enzymic") and factor-dependent systems of translation of polyuridylic acid by Escherichia coli ribosomes. *J Mol Biol* **101**, 537-552, (1976).

44 Katunin, V. I., Savelsbergh, A., Rodnina, M. V. & Wintermeyer, W. Coupling of GTP hydrolysis by elongation factor G to translocation and factor recycling on the ribosome. *Biochemistry* **41**, 12806-12812, (2002).

45 Fredrick, K. & Noller, H. F. Catalysis of ribosomal translocation by sparsomycin. *Science* **300**, 1159-1162, (2003).

46 Salsi, E., Farah, E. & Ermolenko, D. N. EF-G Activation by Phosphate Analogs. *J Mol Biol* **428**, 2248-2258, (2016).

47 Cunha, C. E. *et al.* Dual use of GTP hydrolysis by elongation factor G on the ribosome. *Translation* **1**, e24315:e24315-24311, (2013).

48 Jenner, L. B., Demeshkina, N., Yusupova, G. & Yusupov, M. Structural aspects of messenger RNA reading frame maintenance by the ribosome. *Nat Struct Mol Biol* **17**, 555-560, (2010).

49 Fu, J., Munro, J. B., Blanchard, S. C. & Frank, J. Cryoelectron microscopy structures of the ribosome complex in intermediate states during tRNA translocation. *Proc Natl Acad Sci U S A* **108**, 4817-4821, (2011).

50 Desai, N. *et al.* Elongational stalling activates mitoribosome-associated quality control. *Science* **370**, 1105-1110, (2020).

51 Ranjan, N. *et al.* Yeast translation elongation factor eEF3 promotes late stages of tRNA translocation. *EMBO J* **40**, e106449, (2021).

52 Julian, P. *et al.* Structure of ratcheted ribosomes with tRNAs in hybrid states. *Proc Natl Acad Sci U S A* **105**, 16924-16927, (2008).

53 Loveland, A. B., Demo, G. & Korostelev, A. A. Cryo-EM of elongating ribosome with EF-Tu*GTP elucidates tRNA proofreading. *Nature* **584**, 640-645, (2020).

54 Budkevich, T. *et al.* Structure and dynamics of the mammalian ribosomal pretranslocation complex. *Mol Cell* **44**, 214-224, (2011).

55 Svidritskiy, E., Brilot, A. F., Koh, C. S., Grigorieff, N. & Korostelev, A. A. Structures of Yeast 80S Ribosome-tRNA Complexes in the Rotated and Nonrotated Conformations. *Structure* **22**, 1210-1218, (2014).

56 Korostelev, A., Trakhanov, S., Laurberg, M. & Noller, H. F. Crystal structure of a 70S ribosome-tRNA complex reveals functional interactions and rearrangements. *Cell* **126**, 1065-1077, (2006).

57 Ratje, A. H. *et al.* Head swivel on the ribosome facilitates translocation by means of intra-subunit tRNA hybrid sites. *Nature* **468**, 713-716, (2010).

58 Spahn, C. M. *et al.* Domain movements of elongation factor eEF2 and the eukaryotic 80S ribosome facilitate tRNA translocation. *EMBO J* **23**, 1008-1019, (2004).

59 Flis, J. *et al.* tRNA Translocation by the Eukaryotic 80S Ribosome and the Impact of GTP Hydrolysis. *Cell Rep* **25**, 2676-2688 e2677, (2018).

60 Abeyrathne, P. D., Koh, C. S., Grant, T., Grigorieff, N. & Korostelev, A. A. Ensemble cryo-EM uncovers inchworm-like translocation of a viral IRES through the ribosome. *Elife* **5**, (2016).

61 Guo, Z. & Noller, H. F. Rotation of the head of the 30S ribosomal subunit during mRNA translocation. *Proc Natl Acad Sci U S A* **109**, 20391-20394, (2012).

62 Czworkowski, J., Wang, J., Steitz, T. A. & Moore, P. B. The crystal structure of elongation factor G complexed with GDP, at 2.7 A resolution. *EMBO J* **13**, 3661-3668, (1994).

63 Ogle, J. M. *et al.* Recognition of cognate transfer RNA by the 30S ribosomal subunit. *Science* **292**, 897-902, (2001).

64 Loveland, A. B., Demo, G., Grigorieff, N. & Korostelev, A. A. Ensemble cryo-EM elucidates the mechanism of translation fidelity. *Nature* **546**, 113-117, (2017).

65 Fislage, M. *et al.* Cryo-EM shows stages of initial codon selection on the ribosome by aa-tRNA in ternary complex with GTP and the GTPase-deficient EF-TuH84A. *Nucleic Acids Res* **46**, 5861-5874, (2018).

66 Demeshkina, N., Jenner, L., Westhof, E., Yusupov, M. & Yusupova, G. A new understanding of the decoding principle on the ribosome. *Nature* **484**, 256-259, (2012).

67 Salsi, E., Farah, E., Netter, Z., Dann, J. & Ermolenko, D. N. Movement of elongation factor G between compact and extended conformations. *J Mol Biol* **427**, 454-467, (2015).

68 Chen, Y., Koripella, R. K., Sanyal, S. & Selmer, M. Staphylococcus aureus elongation factor G--structure and analysis of a target for fusidic acid. *FEBS J* **277**, 3789-3803, (2010).

69 Connell, S. R. *et al.* Structural basis for interaction of the ribosome with the switch regions of GTP-bound elongation factors. *Mol Cell* **25**, 751-764, (2007).

70 Chen, J., Sawyer, N. & Regan, L. Protein-protein interactions: general trends in the relationship between binding affinity and interfacial buried surface area. *Protein Sci* **22**, 510-515, (2013).

71 Lancaster, L., Lambert, N. J., Maklan, E. J., Horan, L. H. & Noller, H. F. The sarcin-ricin loop of 23S rRNA is essential for assembly of the functional core of the 50S ribosomal subunit. *RNA* **14**, 1999-2012, (2008).

72 Clementi, N., Chirkova, A., Puffer, B., Micura, R. & Polacek, N. Atomic mutagenesis reveals A2660 of 23S ribosomal RNA as key to EF-G GTPase activation. *Nat Chem Biol* **6**, 344-351, (2010).

73 Koch, M. *et al.* Role of a ribosomal RNA phosphate oxygen during the EF-G-triggered GTP hydrolysis. *Proc Natl Acad Sci U S A* **112**, E2561-2568, (2015).

74 Shi, X., Khade, P. K., Sanbonmatsu, K. Y. & Joseph, S. Functional role of the sarcin-ricin loop of the 23S rRNA in the elongation cycle of protein synthesis. *J Mol Biol* **419**, 125-138, (2012).

75 al-Karadaghi, S., Aevarsson, A., Garber, M., Zheltonosova, J. & Liljas, A. The structure of elongation factor G in complex with GDP: conformational flexibility and nucleotide exchange. *Structure* **4**, 555-565, (1996).

76 Evarsson, A. *et al.* Three-dimensional structure of the ribosomal translocase: elongation factor G from Thermus thermophilus. *Embo J* **13**, 3669-3677, (1994).

77 Voorhees, R. M., Schmeing, T. M., Kelley, A. C. & Ramakrishnan, V. The mechanism for activation of GTP hydrolysis on the ribosome. *Science* **330**, 835-838, (2010).

78 Fenwick, M. K. & Ealick, S. E. Structural basis of elongation factor 2 switching. *Current Research in Structural Biology* **2**, 25-34, (2020).

79 Pasqualato, S. & Cherfils, J. Crystallographic evidence for substrate-assisted GTP hydrolysis by a small GTP binding protein. *Structure* **13**, 533-540, (2005).

80 Savelsbergh, A. *et al.* An elongation factor G-induced ribosome rearrangement precedes tRNA-mRNA translocation. *Mol Cell* **11**, 1517-1523, (2003).

81 Koripella, R. K. *et al.* A conserved histidine in switch-II of EF-G moderates release of inorganic phosphate. *Sci Rep* **5**, 12970, (2015).

82 Ermolenko, D. N. *et al.* Observation of intersubunit movement of the ribosome in solution using FRET. *J Mol Biol* **370**, 530-540, (2007).

83 Stanley, R. E., Blaha, G., Grodzicki, R. L., Strickler, M. D. & Steitz, T. A. The structures of the anti-tuberculosis antibiotics viomycin and capreomycin bound to the 70S ribosome. *Nat Struct Mol Biol* **17**, 289-293, (2010).

84 Peske, F., Savelsbergh, A., Katunin, V. I., Rodnina, M. V. & Wintermeyer, W. Conformational changes of the small ribosomal subunit during elongation factor G-dependent tRNA-mRNA translocation. *J Mol Biol* **343**, 1183-1194, (2004).

85 Modolell, J. & Vazquez. The inhibition of ribosomal translocation by viomycin. *Eur J Biochem* **81**, 491-497, (1977).

86 Dubiez, E., Aleksandrov, A., Lazennec-Schurdevin, C., Mechulam, Y. & Schmitt, E. Identification of a second GTP-bound magnesium ion in archaeal initiation factor 2. *Nucleic Acids Res* **43**, 2946-2957, (2015).

87 Ticu, C., Nechifor, R., Nguyen, B., Desrosiers, M. & Wilson, K. S. Conformational changes in switch I of EF-G drive its directional cycling on and off the ribosome. *EMBO J* **28**, 2053-2065, (2009).

88 Adio, S. *et al.* Fluctuations between multiple EF-G-induced chimeric tRNA states during translocation on the ribosome. *Nat Commun* **6**, 7442, (2015).

89 Fei, J., Kosuri, P., MacDougall, D. D. & Gonzalez, R. L., Jr. Coupling of ribosomal L1 stalk and tRNA dynamics during translation elongation. *Mol Cell* **30**, 348-359, (2008).

90 Chen, C. *et al.* Single-molecule fluorescence measurements of ribosomal translocation dynamics. *Mol Cell* **42**, 367-377, (2011).

91 Pan, D., Kirillov, S. V. & Cooperman, B. S. Kinetically competent intermediates in the translocation step of protein synthesis. *Mol Cell* **25**, 519-529, (2007).

92 Liu, G. *et al.* EF-G catalyzes tRNA translocation by disrupting interactions between decoding center and codon-anticodon duplex. *Nat Struct Mol Biol* **21**, 817-824, (2014).

93 Salsi, E., Farah, E., Dann, J. & Ermolenko, D. N. Following movement of domain IV of elongation factor G during ribosomal translocation. *Proc Natl Acad Sci U S A* **111**, 15060-15065, (2014).

94 Rodnina, M. V., Savelsbergh, A. & Wintermeyer, W. Dynamics of translation on the ribosome: molecular mechanics of translocation. *FEMS Microbiol Rev* **23**, 317-333, (1999).

95 Hirose, K., Akimaru, E., Akiba, T., Endow, S. A. & Amos, L. A. Large conformational changes in a kinesin motor catalyzed by interaction with microtubules. *Mol Cell* **23**, 913-923, (2006).

96 Hwang, W. & Karplus, M. Structural basis for power stroke vs. Brownian ratchet mechanisms of motor proteins. *Proc Natl Acad Sci U S A* **116**, 19777-19785, (2019).

97 Kato, Y., Miyakawa, T. & Tanokura, M. Overview of the mechanism of cytoskeletal motors based on structure. *Biophys Rev* **10**, 571-581, (2018).

98 Ruegg, C. *et al.* Molecular motors: force and movement generated by single myosin II molecules. *News Physiol Sci* **17**, 213-218, (2002).

99 Son, H., Mo, W., Park, J., Lee, J. W. & Lee, S. Single-Molecule FRET Detection of Sub-Nanometer Distance Changes in the Range below a 3-Nanometer Scale. *Biosensors (Basel)* **10**, (2020).

100 Schuwirth, B. S. *et al.* Structures of the bacterial ribosome at 3.5 A resolution. *Science* **310**, 827-834, (2005).

101 Zhou, J., Lancaster, L., Donohue, J. P. & Noller, H. F. Spontaneous ribosomal translocation of mRNA and tRNAs into a chimeric hybrid state. *Proc Natl Acad Sci U S A* **116**, 7813-7818, (2019).

102 Hong, S. *et al.* Mechanism of tRNA-mediated +1 ribosomal frameshifting. *Proc Natl Acad Sci U S A* **115**, 11226-11231, (2018).

103 Horan, L. H. & Noller, H. F. Intersubunit movement is required for ribosomal translocation. *Proc Natl Acad Sci U S A* **104**, 4881-4885, (2007).

104 Selmer, M. *et al.* Structure of the 70S ribosome complexed with mRNA and tRNA. *Science* **313**, 1935-1942, (2006).

105 Gamper, H. *et al.* Insights into genome recoding from the mechanism of a classic +1-frameshifting tRNA. *Nat Commun* **12**, 328, (2021).

106 Gamper, H. B., Masuda, I., Frenkel-Morgenstern, M. & Hou, Y. M. Maintenance of protein synthesis reading frame by EF-P and m(1)G37-tRNA. *Nat Commun* **6**, 7226, (2015).

107 Kaledhonkar, S. *et al.* Late steps in bacterial translation initiation visualized using time-resolved cryo-EM. *Nature* **570**, 400-404, (2019).

108 Hussain, T., Llacer, J. L., Wimberly, B. T., Kieft, J. S. & Ramakrishnan, V. Large-Scale Movements of IF3 and tRNA during Bacterial Translation Initiation. *Cell* **167**, 133-144 e113, (2016).

109 Svidritskiy, E., Demo, G., Loveland, A. B., Xu, C. & Korostelev, A. A. Extensive Ribosome and RF2 Rearrangements during Translation Termination *Elife*, (2019).

110 Fu, Z. *et al.* The structural basis for release-factor activation during translation termination revealed by time-resolved cryogenic electron microscopy. *Nat Commun* **10**, 2579, (2019).

111 Graf, M. *et al.* Visualization of translation termination intermediates trapped by the Apidaecin 137 peptide during RF3-mediated recycling of RF1. *Nat Commun* **9**, 3053, (2018).

112 Fu, Z. *et al.* Key Intermediates in Ribosome Recycling Visualized by Time-Resolved Cryoelectron Microscopy. *Structure* **24**, 2092-2101, (2016).

113 Melnikov, S. *et al.* One core, two shells: bacterial and eukaryotic ribosomes. *Nat Struct Mol Biol* **19**, 560-567, (2012).

114 Noller, H. F. RNA structure: reading the ribosome. *Science* **309**, 1508-1514, (2005).

115 Aibara, S., Singh, V., Modelska, A. & Amunts, A. Structural basis of mitochondrial translation. *Elife* **9**, (2020).

116 Kummer, E. & Ban, N. Structural insights into mammalian mitochondrial translation elongation catalyzed by mtEFG1. *EMBO J* **39**, e104820, (2020).

117 Moazed, D. & Noller, H. F. Transfer RNA shields specific nucleotides in 16S ribosomal RNA from attack by chemical probes. *Cell* **47**, 985-994, (1986).

118 Moazed, D. & Noller, H. F. Interaction of tRNA with 23S rRNA in the ribosomal A, P, and E sites. *Cell* **57**, 585-597, (1989).

119 von Ehrenstein, G. Isolation of sRNA from intact Escherichia coli cells. *Methods in Enzymology* **12**, 588-596, (1967).

120 Yokogawa, T., Kitamura, Y., Nakamura, D., Ohno, S. & Nishikawa, K. Optimization of the hybridization-based method for purification of thermostable tRNAs in the presence of tetraalkylammonium salts. *Nucleic Acids Res* **38**, e89, (2010).

121 Mastronarde, D. N. Automated electron microscope tomography using robust prediction of specimen movements. *J Struct Biol* **152**, 36-51, (2005).

122 Kremer, J. R., Mastronarde, D. N. & McIntosh, J. R. Computer visualization of three-dimensional image data using IMOD. *J Struct Biol* **116**, 71-76, (1996).

123 Grant, T., Rohou, A. & Grigorieff, N. cisTEM, user-friendly software for single-particle image processing. *Elife* **7**, (2018).

124 Grigorieff, N. Frealign: An Exploratory Tool for Single-Particle Cryo-EM. *Methods Enzymol* **579**, 191-226, (2016).

125 Demo, G. *et al.* Mechanism of ribosome rescue by ArfA and RF2. *Elife* **6**, (2017).

126 Cardone, G., Heymann, J. B. & Steven, A. C. One number does not fit all: mapping local variations in resolution in cryo-EM reconstructions. *J Struct Biol* **184**, 226-236, (2013).

127 Pettersen, E. F. *et al.* UCSF Chimera--a visualization system for exploratory research and analysis. *J Comput Chem* **25**, 1605-1612, (2004).

128 The PyMOL Molecular Graphics System v. The PyMOL Molecular Graphics System (DeLano Scientific, Palo Alto, CA, USA, 2002).

129 Chapman, M. S. Restrained real-space macromolecular atomic refinement using a new resolution-dependent electron density function. *Acta Crystallogr. A* **51**, 69-80, (1995).

130 Korostelev, A., Bertram, R. & Chapman, M. S. Simulated-annealing real-space refinement as a tool in model building. *Acta Crystallogr D Biol Crystallogr* **58**, 761-767, (2002).

131 Korostelev, A. *et al.* Crystal structure of a translation termination complex formed with release factor RF2. *Proc Natl Acad Sci U S A* **105**, 19684-19689, (2008).

132 Adams, P. D. *et al.* PHENIX: a comprehensive Python-based system for macromolecular structure solution. *Acta Crystallogr D Biol Crystallogr* **66**, 213-221, (2010).

133 Chen, V. B. *et al.* MolProbity: all-atom structure validation for macromolecular crystallography. *Acta Crystallogr D Biol Crystallogr* **66**, 12-21, (2010).